Ground-state and excited-state properties of $LaMnO_3$ from full-potential calculations

P. Ravindran,[1,*] A. Kjekshus,[1] H. Fjellvåg,[1] A. Delin,[2] and O. Eriksson[3]
[1]*Department of Chemistry, University of Oslo, Box 1033, Blindern, N-0315, Oslo, Norway*
[2]*ICTP, Strada Costiera 11, P.O. Box 586, 34100, Trieste, Italy*
[3]*Condensed Matter Theory Group, Department of Physics, Uppsala University, Box 530, 75121, Uppsala, Sweden*
(Received 29 March 2001; published 24 January 2002)

The ground-state and excited-state properties of the perovskite $LaMnO_3$, the mother material of colossal magnetoresistance manganites, are calculated based on the generalized-gradient-corrected relativistic full-potential method. The electronic structure, magnetism, and energetics of various spin configurations for $LaMnO_3$ in the ideal cubic perovskite structure and the experimentally observed distorted orthorhombic structure are obtained. The excited-state properties such as the optical, magneto-optical, x-ray photoemission, bremsstrahlung isochromat, and x-ray absorption near-edge structure spectra are calculated and found to be in excellent agreement with available experimental results. Consistent with earlier observations the insulating behavior can be obtained only when we take into account the structural distortions and the correct antiferromagnetic ordering in the calculations. The present results suggest that the correlation effect is not significant in $LaMnO_3$ and the presence of ferromagnetic coupling within the ab plane as well as the antiferromagnetic coupling perpendicular to this plane can be explained through the itinerant band picture. Our calculations show that the Mn $3d$ e_g-like electrons are present in the whole valence-band region. We have calculated the hyperfine field parameters for the *A*-type antiferromagnetic and the ferromagnetic phases of $LaMnO_3$ and compared the findings with the available experimental results. The role of the orthorhombic distortion on electronic structure, magnetism, and optical anisotropy is analyzed.

DOI: 10.1103/PhysRevB.65.064445 PACS number(s): 78.20.Ls, 78.20.Ci, 74.25.Gz

I. INTRODUCTION

Even though the Mn containing oxides with perovskite-like structure have been studied for more than a half century,[1,2] various phase transitions occurring on doping in these materials are not fully understood. In particular, $LaMnO_3$ exhibits rich and interesting physical properties because of the strong interplay between lattice distortions, transport properties, and magnetic ordering. This compound also has a very rich phase diagram depending on the doping concentration, temperature, and pressure, being either an antiferromagnetic (AF) insulator, ferromagnetic (F) metal, or charge-ordered (CO) insulator.[3] The magnetic behavior of the $LaMnO_3$ perovskite is particularly interesting, because the Jahn-Teller (JT) distortion is accompanied by the so-called *A*-type antiferromagnetic (*A*-AF) spin (moment) and *C*-type orbital ordering (OO), i.e., alternative occupation of $d_{x^2-r^2}$ and $d_{y^2-r^2}$ in the ab plane and the same type of orbital occupation perpendicular to the ab plane.[4] Recently manganites have also been subjected to strong interest due to their exhibition of negative colossal magnetoresistance (CMR) effects.[5] In particular the perovskite-oxide system $La_{1-x}A_xMnO_3$, where *A* is a divalent alkali element such as Ca or Sr, has attracted much attention primarily due to the discovery of a negative CMR effect around the ferromagnetic transition temperature T_C, which is located near room temperature.[5] The mutual coupling among the charge, spin, orbital, and lattice degrees of freedom in perovskite-type manganites creates versatile intriguing phenomena such as CMR,[5] field melting of the CO and/or OO state(s) accompanying a huge change in resistivity,[6] field-induced structural transitions even near room temperature,[7] field control of intergrain or interplane tunneling of highly spin-polarized carriers,[8] etc. Several mechanisms have been proposed for CMR, such as double exchange,[9] dynamical JT effect,[10] antiferromagnetic fluctuation,[11] etc., but no consensus has been attained so far about the importance of those mechanisms. Since the spin, charge, orbital, and structural ordering phenomena may affect CMR at least indirectly it is important to obtain a full understanding of the mechanism stabilizing the observed *A*-AF order in the undoped insulating mother compound $LaMnO_3$.

It has been suggested that an understanding of hole-doped $LaMnO_3$ must include, in addition to the double-exchange mechanism,[9] strong electron correlations,[12] a strong electron-phonon interaction,[13] and cooperative JT distortions associated with Mn^{3+}. Several theoretical studies have been made on this material using the mean-field approximation,[14,15] numerical diagonalization,[16] Gutzwiller technique,[17] slave-fermion theory,[18] dynamical mean-field theory,[19,20] perturbation theory,[21] and quantum Monte Carlo technique.[22] Nevertheless, it is still controversial as to what is the driving mechanism of the experimentally established properties, particularly the strongly incoherent charge dynamics, and what the realistic parameters of theoretical models are. By calculating and comparing various experimentally observed quantities one can get an idea about the role of electron correlations and other influences on the CMR effect in these materials. Hence, theoretical investigations of ground-state and excited state properties are important to understand the exotic physical properties of these materials.

The importance of spin and lattice degrees of freedom on the metal-insulator transition in $LaMnO_3$ has been studied extensively.[23] Popovic and Satpathy[24] showed how the cooperative JT coupling between the individual MnO_6 centers in the crystal leads to simultaneous ordering of the distorted

octahedron and the electronic orbitals. It is now accepted that OO and magnetic ordering (MO) are closely correlated and that the anisotropy in the magnetic coupling originates from OO.[25] So in order to understand the origin of OO, it is important to study the energetics of different spin-ordered states. Ahn and Millis[26] calculated the optical conductivity of $LaMnO_3$ using a tight-binding parametrization of the band structure. They noted a troubling discrepancy with local spin-density approximation (LSDA) band-theory calculations[27] of the optical conductivity and concluded with the need for further work to find the origin of the difference. Hence, accurate calculations of optical properties is expected to give more insight into the origin of the discrepancy. An appreciable Faraday rotation has been observed in hole-doped $LaMnO_3$ thin films[28] and hence it has been suggested that these ferromagnetic films may be used to image vortices in high-temperature superconductors. Further, due to the half-metallic behavior of the F phase of $LaMnO_3$, one can expect a large magneto-optical effect. For this reason, we have calculated the optical and magneto-optical properties of this material.

The density-functional calculations often fail[29,30] to predict the insulating behavior of $LaMnO_3$. To correct this deficiency of the LSDA to give the right insulating properties of the perovskites, LSDA+U theory[31,32] is applied, where U is the intrasite Coulomb repulsion. From experimental and theoretical studies it has been believed that the electron correlations in the LaTO$_3$ (T=Ti–Cu) series are very important and should be considered more rigorously beyond the LSDA. Hence, LDA+U is applied[27] to obtain magnetic moments and fundamental gaps in good agreement with experiment. The calculations for LaTO$_3$ by Solovyev *et al.*[27] showed that the correlation correction was significant for Ti, V, and Co but less important for Mn. However, in this study the calculated intensity of the optical conductivity was found to be much smaller than the experimental results in the whole energy range. Hu *et al.*[33] reported that to get the correct experimental ground state for $LaMnO_3$, it is necessary to take JT distortion, electron-electron correlation, and AF ordering simultaneously into consideration. From the observation of large on-site Coulomb U and exchange J, obtained from ''constrained LDA calculations'', Satpathy *et al.*[34] indicated the importance of correlation effects in $LaMnO_3$. Held and Vollhardt,[35] using the dynamical mean-field theory, emphasize the importance of electronic correlations from the local Coulomb repulsion for understanding the properties of manganites. Maezono *et al.*[15] pointed out that the electron correlations remain strong even in the metallic state of doped manganites. Photoemission studies on doped manganites gave an electron-electron correlation effect with $U=7.5$ eV for the Coulomb repulsion.[36,37]

Many aspects of the ground-state as well as single-electron excited-state properties of $LaMnO_3$ and related compounds can be described satisfactorily in terms of LSDA energy bands.[38–40] Density-functional calculations also show strong couplings between lattice distortions, magnetic order, and electronic properties of $LaMnO_3$. In particular, it is found that without lattice distortions $LaMnO_3$ would have a F metallic ground state, and even if forced to be A-AF, it would still be metallic.[39] Further, Sarma *et al.*[38] indicated that the electron-electron correlation is unimportant due to a relatively large hopping parameter t and a large screening effect. LSDA studies[34,39–42] show that substantially hybridized bands derived from majority-spin Mn e_g and O p states dominate the electronic structure near the Fermi energy (E_F). X-ray absorption spectroscopy (XAS) data show that several apparent peaks exist up to 5 eV above E_F, but some disputes still remain about the origins of these conduction-band peaks.[43–45] The reported positions of the $e_g^{1\uparrow}$ bands in $LaMnO_3$ differ.[34,45] The above-mentioned studies indicate that it is important to study the significance of correlation effects in $LaMnO_3$.

Some of the features lacking in most of the theoretical studies on $LaMnO_3$ originate from the fact that they have often resulted from use of the atomic-sphere approximation (ASA); i.e., the calculations have not included the nonspherical part of the potential and also used a minimal basis set. Further the cubic perovskite structure is frequently assumed,[29,46] neglecting significant structural distortions. Apart from these, owing to the presence of magnetic ordering, relativistic effects such as spin-orbit coupling may be of significance in this material, which has not been included in earlier studies. Moreover, it is shown that instead of using the uniform electron gas limit for exchange and correlations (corresponding to the LSDA) one can improve the outcome by including inhomogeneity effects through the generalized-gradient approximation (GGA).[47] To overcome the above mentioned deficiencies we have used a generalized-gradient-corrected, relativistic full-potential method with the experimentally observed orthorhombic distorted perovskite structure as the input in the present calculation.

The rest of the paper is organized as follows. Structural aspects and computational details about the calculations of the electronic structure, energetics of different magnetic phases, optical properties, magneto-optical properties, x-ray photoemission spectrum (XPS), and x-ray absorption near-edge structure (XANES) features are given in Sec. II. In Sec. III we give the orbital, angular momentum, and site-projected density of states (DOS) for $LaMnO_3$ in the ground state, and the spin-projected DOS for various magnetic states. The calculated band structures for the A-AF and F phases of the distorted orthorhombic structure are given. The role of the structural distortion on the electronic structure, optical, and magnetic properties is analyzed. Calculated magnetic properties are compared with available experimental and theoretical studies. The origin of excited-state properties such as XPS, bremsstrahlung isochromat spectrum (BIS), XANES, optical properties, and magneto-optical properties is analyzed through the electronic structure and compared with available experimental spectra. Finally in Sec. IV we have summarized the important findings of the present study.

II. STRUCTURAL ASPECTS AND COMPUTATIONAL DETAILS

A. Crystal and magnetic structure

$LaMnO_3$ is stabilized in the orthorhombic $GdFeO_3$-type structure[48,49] (comprising four formula units, space group $Pnma$) as shown in Fig. 1. It can be viewed as a highly

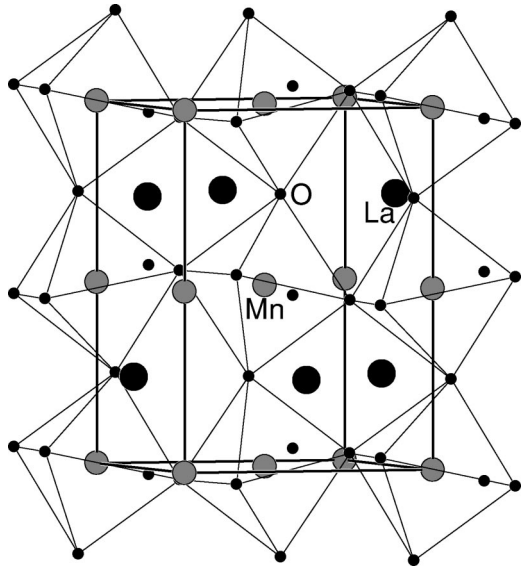

FIG. 1. The $GdFeO_3$-type crystal structure of $LaMnO_3$, viz., an orthorhombically distorted perovskite-type structure.

distorted cubic perovskite structure with a quadrupled unit cell ($a_p\sqrt{2}$, $2a_p$, $a_p\sqrt{2}$) where a_p is the lattice parameter of the cubic perovskite structure. The structural parameters used in the calculations are taken from a 4.2 K neutron diffraction study:[49] $a=5.742$ Å, $b=7.668$ Å, and $c=5.532$ Å and atom positions La in $4c$ (0.549 0.25 0.01), Mn in $4a$ (0 0 0), O(1) in $4c$ (-0.014 0.25 -0.07), and O(2) in $8d$ (0.309 0.039 0.244). The electronic configuration of Mn^{3+} in $LaMnO_3$ is postulated as $t_{2g}^{3\uparrow}e_g^{1\uparrow}$ and, hence, it is a typical JT system. Basically, two different types of distortions are included in the structure shown in Fig. 1. One is a tilting of the MnO_6 octahedra around the cubic [110] axis as in $GdFeO_3$ so that the Mn-O-Mn angle changes from 180° to ~160° which is not directly related to the JT effect, but is attributed to the relative sizes of the components, say, expressed in terms of the tolerance factor $t_p=(R_{La}+R_O)/[\sqrt{2}(R_{Mn}+R_O)]$, where R_{La}, R_{Mn}, and R_O are the ionic radii for La, Mn, and O, respectively, giving $t_p=0.947$ for $LaMnO_3$. The rotation of the MnO_6 octahedra facilitates a more efficient space filling. The second type of crystal distortion in $LaMnO_3$ is the deformation of the MnO_6 octahedra caused by the JT effect, viz., originating from orbital degeneracy. This may be looked upon as a cooperative shifting of the oxygens within the ab plane away from one of its two nearest-neighboring Mn atoms toward the others, thus creating long and short Mn-O bond lengths (modified from 1.97 Å for the cubic case to 1.91, 1.96, and 2.18 Å for the orthorhombic variant) perpendicularly arranged with respect to the Mn atoms. The long bonds can be regarded as rotated 90° within ab on going from one Mn to the neighboring Mn.[50] The structural optimization[47] wrongly predicts that the ground state of $LaMnO_3$ is close to that of cubic perovskite with the F state lower in energy than the experimentally observed AF state. Hence, it is important to study the relative stability between the orthorhombic and cubic phases for different magnetic arrangements. Consequently we have made calculations both for the orthorhombic ($Pnma$) as well as the ideal cubic perovskite variant. For the calculations for the undistorted cubic variant we have used the experimental equilibrium volume for the orthorhombic structure.

When $LaMnO_3$ is in the AF state there are three possible magnetic arrangements according to interplane and intraplane couplings within the (001) plane. (i) With interplane AF coupling and intraplane F coupling the *A*-AF structure arises. (ii) The opposite structure of *A*-AF, where the interplane coupling is F and the intraplane coupling AF, is called *C*-AF structure. In the *C*-type cell all atoms have two F and four AF nearest neighbors whereas the reverse is true for *A*-AF. (iii) If both the inter- and intraplane couplings are AF, the *G*-AF structure should arise.[46] In the *G*-type AF lattice, each Mn atom is surrounded by six Mn neighbors whose spins are antiparallel to the chosen central atom. Among the several possible magnetic orderings, the experimental studies show that for $LaMnO_3$ the *A*-AF ordering is the ground state with a Néel temperature of 140 K. In the cubic case we have made calculations for the AF structures in the following way. The *A*-AF structure contains two formula units and takes a tetragonal lattice with $a=b=a_p$ and $c=2a_p$. The *C*-AF structure is also tetragonal with $a=b=\sqrt{2}a_p$ and $c=a_p$. Finally, the *G*-AF structure is a face-centered-cubic structure with $a=b=c=2a_p$ with eight formula units, where two nonequivalent $3d$ metals with spins up and down replace Na and Cl in an NaCl configuration. This magnetic structure can be viewed as consisting of two interpenetrating face-centered lattices with opposite spin orientation.

B. Computation details for the LAPW calculations

These investigations are based on *ab initio* electronic structure calculations derived from spin-polarized density-functional theory (DFT). For the XANES, orbital-projected DOS and the screened plasma frequency calculations we have applied the full-potential linearized augmented plane-wave (FPLAPW) method[51] in a scalar-relativistic version, i.e., without spin-orbit (SO) coupling. In the calculation we have used the atomic sphere radii (R_{MT}) of 2.2, 2.0, and 1.5 a.u. for La, Mn, and O, respectively. Since the spin densities are well confined within a radius of about 1.5 a.u., the resulting magnetic moments do not depend strongly on the variation of the atomic sphere radii. The charge density and the potentials are expanded into lattice harmonics up to $l=6$ inside the spheres and into a Fourier series in the interstitial region. The initial basis set included $4s$, $4p$, and $3d$ functions and $3s$ and $3p$ semicore functions at the Mn site, $6s$, $6p$, and $5d$ valence and $5s$ and $5p$ semicore functions for the La site, and $2s$, $2p$, and $3d$ functions for the O sites. This set of basis functions was supplemented with local orbitals for additional flexibility in representing the semicore states and for relaxing the linearization errors generally. Due to the linearization errors, DOS are reliable to about 1–2 Ry above the Fermi level. So after self-consistency was achieved for this basis set we included a few high-energy local orbitals; $6d$- and $4f$-like functions for La, $5s$- and $5p$-like functions for Mn, and $3p$-like functions for O atoms. The effects of exchange and correlation are treated within the generalized-gradient-corrected local spin-density approximation using

the parametrization scheme of Perdew *et al.*[52] To ensure convergence for the Brillouin zone (BZ) integration 243 **k** points in the irreducible wedge of first BZ were used. Self-consistency was achieved by demanding the convergence of the total energy to be smaller than 10^{-5} Ry/cell. This corresponds to a convergence of the charge below 10^{-4} electrons/atom.

C. Computational details for the FPLMTO calculations

The full-potential LMTO calculations[53] presented in this paper are all electron, and no shape approximation to the charge density or potential has been used. The base geometry in this computational method consists of a muffin-tin part and an interstitial part. The basis set is comprised of augmented linear muffin-tin orbitals (LMTO's).[54] Inside the muffin-tin spheres the basis functions, charge density, and potential are expanded in symmetry-adapted spherical harmonic functions together with a radial function and a Fourier series in the interstitial. In the present calculations spherical-harmonic expansion of the charge density, potential, and basis functions was carried out up to $l=6$. The tails of the basis functions outside their parent spheres are linear combinations of Hankel or Neumann functions depending on the sign of the kinetic energy of the basis function in the interstitial region. For the core charge density, the Dirac equation is solved self-consistently; i.e., no frozen core approximation is used. The calculations are based on the generalized-gradient-corrected-density-functional theory as proposed by Perdew *et al.*[52]

The SO term is included directly in the Hamiltonian matrix elements for the part inside the muffin-tin spheres, thus doubling the size of the secular matrix for a spin-polarized calculation. Even though the La $4f$ states are well above E_F, their contributions to the magnetic and structural properties are very important.[47] So we have included these orbitals in all our calculations. Moreover, the present calculations make use of a so-called multibasis to ensure a well-converged wave function. This means that we use different Hankel or Neumann functions, each attaching to its own radial function. We thus have two $6s$, two $5p$, two $6p$, two $5d$, and two $4f$ orbitals for La, two $4s$, two $5p$, and three $3d$ orbitals for Mn, and two $2s$, three $2p$, and two $3d$ orbitals for O in our expansion of the wave function. In the method used here, bases corresponding to multiple principal quantum numbers are contained within a single, fully hybridizing basis set. The direction of the moment is chosen to be (001). The calculations were performed for the cubic perovskite structure as well as the orthorhombic $GdFeO_3$-type structure in nonmagnetic (P), F, *A*-AF, *C*-AF, and *G*-AF states. The **k**-space integration was performed using the special-point method with 284 **k** points in the irreducible part of first BZ for the orthorhombic structure and the same density of **k** points were used for the cubic structure in the actual cell as well as the supercell. All calculations were performed using the experimental structural parameters mentioned in Sec. II A for both the nonmagnetic and spin-polarized cases. Using the self-consistent potentials obtained from our calculations, the imaginary part of the optical dielectric tensor and the band structure of $LaMnO_3$ were calculated for the *A*-AF and F cases. The density of states was calculated for the P, F, *A*-AF, *C*-AF, and *G*-AF phases in the cubic as well as orthorhombic structure using the linear tetrahedron technique.

D. Calculation of optical properties

Once energies $\epsilon_{\mathbf{k}n}$ and functions $|\mathbf{k}n\rangle$ for the n bands are obtained self-consistently, the interband contribution to the imaginary part of the dielectric functions $\epsilon_2(\omega)$ can be calculated by summing transitions from occupied to unoccupied states (with fixed **k** vector) over the BZ, weighted with the appropriate matrix element for the probability of the transition. To be specific, the components of $\epsilon_2(\omega)$ are given by

$$\epsilon_2^{ij}(\omega)=\frac{Ve^2}{2\pi\hbar m^2\omega^2}\int d^3k\sum_{nn'}\langle\mathbf{k}n|p_i|\mathbf{k}n'\rangle\langle\mathbf{k}n'|p_j|\mathbf{k}n\rangle \times f_{\mathbf{k}n}(1-f_{\mathbf{k}n'})\,\delta(\epsilon_{\mathbf{k}n'}-\epsilon_{\mathbf{k}n}-\hbar\omega). \quad (1)$$

Here $(p_x,p_y,p_z)=\mathbf{p}$ is the momentum operator and $f_{\mathbf{k}n}$ is the Fermi distribution. The evaluation of the matrix elements in Eq. (1) is done over the muffin-tin and interstitial regions separately. Further details about the evaluation of matrix elements are given elsewhere.[55] Due to the orthorhombic structure of $LaMnO_3$, the dielectric function is a tensor. By an appropriate choice of the principal axes we can diagonalize it and restrict our considerations to the diagonal matrix elements. We have calculated the three components $E\|a$, $E\|b$, and $E\|c$ of the dielectric constants corresponding to the electric field parallel to the crystallographic axes *a*, *b*, and *c*, respectively. The real part of the components of the dielectric tensor $\epsilon_1(\omega)$ is then calculated using the Kramer-Kronig transformation. Knowledge of both the real and imaginary parts of the dielectric tensor allows the calculation of important optical constants. In this paper, we present the reflectivity $R(\omega)$, the absorption coefficient $I(\omega)$, and the electron energy loss spectrum $L(\omega)$, as well as the refractive index n and the extinction coefficient k. The calculations yield unbroadened functions. To reproduce the experimental conditions more correctly, it is necessary to broaden the calculated spectra. The exact form of the broadening function is unknown, although comparison with measurements suggests that the broadening usually increases with increasing excitation energy. Also the instrumental resolution smears out many fine features. To simulate these effects the lifetime broadening was simulated by convoluting the absorptive part of the dielectric function with a Lorentzian, whose full width at half maximum (FWHM) is equal to $0.01(\hbar\omega)^2$ in eV. The experimental resolution was simulated by broadening the final spectra with a Gaussian, where FWHM is equal to 0.02 eV.

E. Calculation of magneto-optical properties

The magneto-optic effect can be described by the off-diagonal elements of the dielectric tensor which originate from optical transitions with a different frequency dependence of right and left circularly polarized light because of SO splitting of the states involved. For the polar geometry,

the Kerr rotation (θ_K) and ellipticity (η_K) are related to the optical conductivity through the following relation:

$$\frac{1+\tan(\eta_K)}{1-\tan(\eta_K)}e^{2i\theta_K}=\frac{(1+n_+)(1-n_-)}{(1-n_+)(1+n_-)}. \tag{2}$$

$n_\pm^2$ in terms of conductivities is

$$n_\pm^2=1+\frac{4\pi i}{\omega}(\sigma_{xx}\pm i\sigma_{xy}). \tag{3}$$

For small Kerr angles, Eq. (2) can be simplified to[56]

$$\theta_K+i\eta_K=\frac{-\sigma_{xy}}{\sigma_{xx}\sqrt{1+\frac{4\pi i}{\omega}\sigma_{xx}}}. \tag{4}$$

The magnetic circular birefringence, also called the Faraday rotation θ_F, describes the rotation of the polarization plane of linearly polarized light on transmission through matter magnetized in the direction of the light propagation. Similarly, the Faraday ellipticity η_F, which is also known as the magnetic circular dichroism, is proportional to the difference of the absorption for right- and left-handed circularly polarized light.[57] Thus, these quantities are simply given by[58]

$$\theta_F+i\eta_F=\frac{\omega d}{2c}(n_+-n_-), \tag{5}$$

where c is the velocity of light in vacuum and d is the thickness of the thin film.

F. Calculation of XPS and BIS spectra

Within the so-called single-scatterer final-state approximation[59,60] (free propagation of the photoelectrons through the crystal, loss of **k**-dependent information, and neglect of surface effects) the photocurrent is a sum of local (atomic-like) and partial (l-like) DOS weighted by cross sections (transition probabilities). As the theoretical framework of the XPS intensity calculations has been given earlier,[61] only a brief description of the main points is outlined here. For high incident energies of XPS ($\sim$1.5 keV) the low-energy electron-diffraction function[60] can be simplified and the fully relativistic angle-integrated intensity $I(E,\omega)$ can be written as

$$I(E,\omega)=\sum_\tau\sum_\kappa \sigma_\kappa^\tau(E,\omega)D_\kappa^\tau(E)\,\delta(E_F+\hbar\omega-E),$$

$$\kappa=\begin{cases}-l-1 & j=l+\frac{1}{2},\\ l & j=l-\frac{1}{2},\end{cases} \tag{6}$$

where ω denotes the energy of the incident photons. This expression has been cast into a Fermi golden-rule form, where $D_\kappa^\tau(E)$ is the partial DOS function for the κth channel at the τth site, and are obtained from full-potential LMTO calculation. The partial, angular momentum-dependent cross sections $\sigma_\kappa^\tau(E,\omega)$ of the species τ can be obtained from

$$\sigma_\kappa^\tau(E,\omega)=\sum_{\kappa'}(2j+1)\begin{pmatrix} j & 1 & j' \\ \frac{1}{2} & 0 & -\frac{1}{2}\end{pmatrix}^2[M_{kk'}^\tau(E,\omega)]^2,$$

where

$$M_{kk'}^\tau(E,\omega)=\int_0^{R_{mt}}R_\kappa^\tau(r_\tau,E)\nabla V^\tau(r_\tau)Z_{\kappa'}^\tau(r_\tau,\omega)r_\tau^2dr_\tau. \tag{7}$$

In Eq. (7) the radial functions $R_\kappa^\tau(r_\tau,E)$ and $Z_{\kappa'}^\tau(r_\tau,E)$ differ conceptually only by different single-site scattering normalizations. The radial gradient $\nabla V^\tau(r_\tau)$ refer to the τth scattering potential. The Wigner $3j$ symbols

$$\begin{pmatrix} j & 1 & j' \\ \frac{1}{2} & 0 & -\frac{1}{2}\end{pmatrix}$$

automatically take care of the dipole selection rules. The relativistic cross sections $\sigma_\kappa^\tau(E,\omega)$ are calculated using the muffin-tin part of the potential over the energy range E of the DOS functions for the fixed incident photon energy ω. This expression has been evaluated for $LaMnO_3$ from the potentials and DOS functions by a fully relativistic full-potential LMTO self-consistent calculation. Because the cross sections (matrix elements) are energy dependent, the theoretically predicted spectra will depend on the energy chosen for the calculation. To be consistent with the reported XPS data, we have made all calculations with the fixed incident photon energy $\omega=1253.6$ eV (Mg $K\alpha$ line) used in the experimental study. The finite lifetime of the photoholes was taken into account approximately by convoluting the spectra using a Lorentzian with an energy-dependent halfwidth. The FWHM of this Lorentzian is zero at E_F and increases linearly with the binding energy, as $0.2(E_F-E)$. In addition to the Lorentzian lifetime broadening, the spectra were broadened with a Gaussian of half-width 0.8 eV to account for spectrometer resolution. The procedure we adapt to calculate XPS and BIS spectra is as follows. First, we take the partial DOS functions ($E<E_F$ for XPS and $E>E_F$ for BIS) from full-potential LMTO calculations. We multiply these by the calculated l-dependent cross sections for all band energies and sum them to get a total spectral-like function. Next, to get a good fit to the data we broaden this with an energy-dependent Lorentzian function to simulate what we call inherent lifetime effects due to the coupling of the excited outgoing electron from the crystal. This broadening is zero at E_F and goes as the square of the energy below E_F. Then we fit the leading edge to the experimental data with a Gaussian broadening to simulate the instrument resolution. This broadening is the same for all states. Finally we add a background function to get the experimental profile. While the calculations were performed at the one-electron level, we believe this procedure should capture the essence of the photoemission process and lead to a meaningful comparison between calculated and observed spectra.

G. Calculation of XANES

The theoretical x-ray absorption spectra for $LaMnO_3$ were computed within the dipole approximation from the FLAPW (Ref. 51) partial DOS along the lines described by Neckel *et al.*[62] The intensity $I(\omega)=E-E_c$ arising from transitions from initial valence-band (VB) states (energy E and an angular momentum l) to a final core state (E_c,l') is given by

$$\frac{I_{\tau n'l'}(\omega)}{\omega^3}=\sum_l W_{ll'}M^2_\tau(l,n'l',E)D^\tau_l(E)\,\delta(E-E^{core}_{n'l'}-\hbar\omega), \tag{8}$$

where the matrix elements are given by

$$M^2_\tau(l,n'l',E)=\frac{\left[\int_0^{R_\tau}P^\tau_l(r,E)rP_{n'l'prime}(r)dr\right]^2}{\int_0^{R_\tau}P_{l\tau}(r,E)^2dr}.$$

Here n' and l' represent principal and angular momentum quantum numbers for the core states. $D^\tau_l(E)$ is the partial DOS of atom τ with angular momentum l; P^τ_l and R_τ are the radial wave function and atomic sphere radius of atom τ. The transition coefficient $W_{ll'}$ can be calculated analytically according to the following equation:

$$W_{ll'}=\frac{l+1}{2l+1}\delta_{l,l'-1}+\frac{l}{2l-1}\delta_{l,l'+1}.$$

For absorption spectra $D^\tau_l(E>E_F)=0$. To account for instrumental resolution and lifetime broadening of core and valence states we have broadened the calculated spectra using the Lorentzian function with FWHM of 1 eV.

III. RESULTS AND DISCUSSION

A. Electronic structure

1. Electronic structure of the cubic phase

Let us first discuss qualitative distinctions among the electronic band structures of $LaMnO_3$ with various magnetic configurations without considering the structural distortion. With full cubic symmetry, t_{2g} and e_g orbitals are three- and twofold degenerate, respectively. The orbital-projected DOS for Mn $3d$ electrons in the F phase of cubic $LaMnO_3$ are shown in Fig. 2, where the t_{2g} states are away from E_F and also rather narrow. However, the e_g levels are broadly distributed within the DOS profile. The electrons at E_F have both $e_g^\uparrow$ and $t_{2g}^\downarrow$ electrons as shown in Fig. 2. Against the pure ionic picture (where only the e_g electrons are expected to be closer to E_F) there is considerable amount of e_g electrons present around -6 eV. These states originate from the covalent interaction between the Mn e_g electrons and O $2p$ states which produce the e_g bonding (around -6 eV) and antibonding (above -2 eV) hybrids. The t_{2g} states are energetically degenerate with the O $2p$ states in the VB, indicating that there are finite covalent interactions between these states. Owing to this covalent interaction along with the exchange interaction between the t_{2g} and e_g states, a finite DOS of t_{2g} electrons in the energy range -7 to -5 eV is created. With E_F positioned in the middle of the e_g band, a JT instability is produced which causes the oxygen octahedra to distort and removes the orbital degeneracy. For the undistorted cubic perovskite structure, the total DOS is shown in Fig. 3 for the nonmagnetic (paramagnetic=P), F,

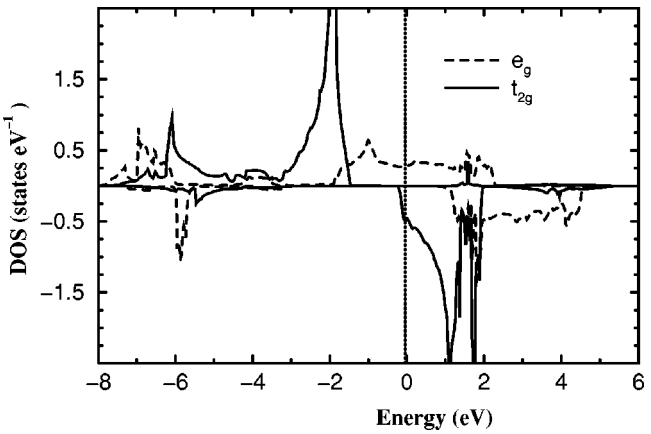

FIG. 2. Orbital projected DOS for Mn in F-state $LaMnO_3$ with hypothetical cubic perovskite structure (obtained by LAPW calculations).

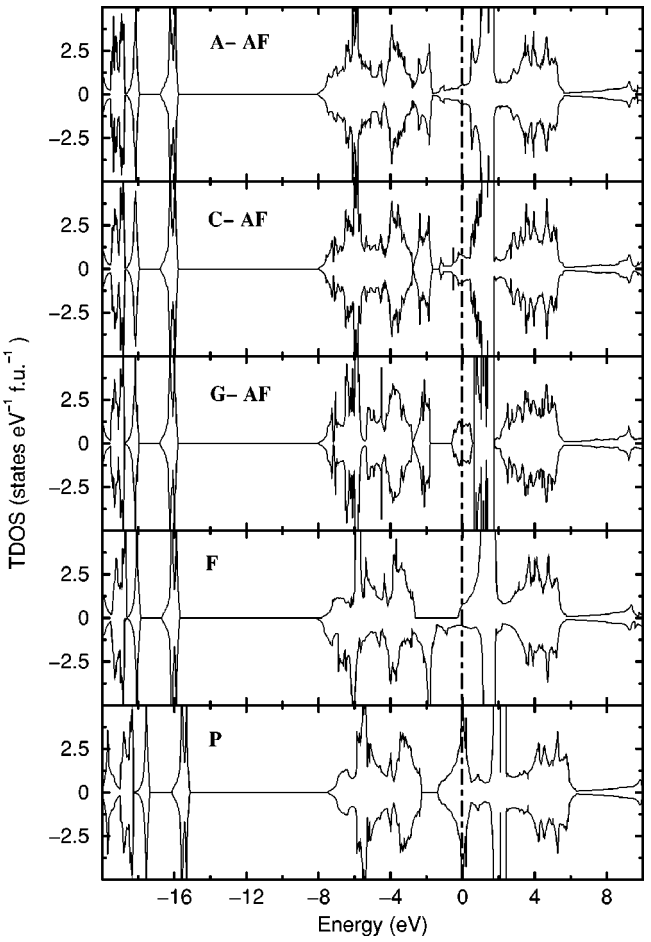

FIG. 3. Total DOS for $LaMnO_3$ in cubic perovskite-type atomic arrangement and P, F, and *A*-, *C*-, and *G*-AF magnetic states.

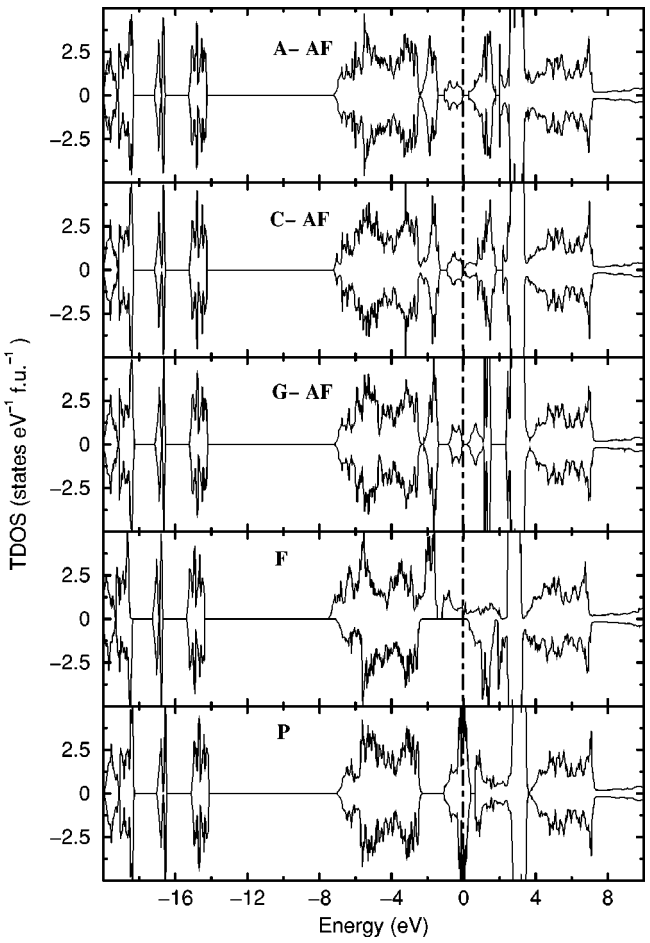

FIG. 4. Total DOS for $LaMnO_3$ in orthorhombic $GdFeO_3$-type structure and P, F, and *A*-, *C*-, and *G*-AF magnetic states.

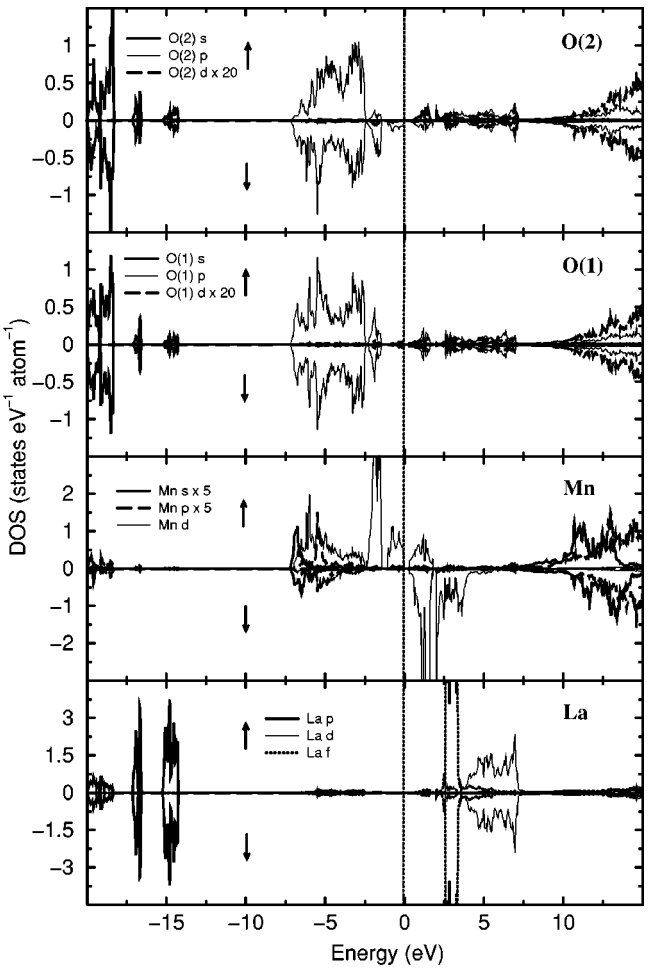

FIG. 5. Site and angular-momentum-projected DOS for *A*-AF-state $LaMnO_3$ with orthorhombic $GdFeO_3$-type structure.

and *A*-, *C*-, and *G*-type AF spin configurations. Without the JT-caused lattice distortion, the LSDA calculations show that $LaMnO_3$ is metallic for all these magnetic states. In all the cooperative magnetic states, the Hund splitting is large and induces an empty minority-spin band at the Mn site. From DOS for the F state of the undistorted structure (see Fig. 3) one can see that there is a finite number of states present in both spin channels. On the other hand, the half-metallic character clearly appeared in the F state of the orthorhombic structure (Fig. 4). The different hybridization nature of the cubic and orthorhombic phases and the noninvolvement of JT effects in the cubic phase are the possible reasons for the absence of the half-metallic character in the cubic phase. The total DOS of the AF phases are much different from that of the F phase (Fig. 3). Owing to large exchange splitting, there is a smaller DOS at the Fermi level $[N(E_F)]$ for the F and AF phases compared with the P phase. The calculated value of $N(E_F)$ for the P phase is 146.6 states/(Ry f.u.) and 16.7, 20.5, 25.1, and 17.8 states/(Ry f.u.) for *A*-, *C*-, *G*-AF, and F phases, respectively.

2. Electronic structure of the orthorhombic phase

Let us now focus on the role of the structural distortion on the electronic structure of $LaMnO_3$. The important factors governing the formation of the electronic structure of orthorhombic $LaMnO_3$ are the exchange splitting owing to spin polarization, the ligand field splitting of e_g and t_{2g} states, and the further splitting of the e_g states owing to the JT distortion. It is believed that $LaMnO_3$ is a charge-transfer-type (CT-type) insulator[45,63] according to the Zaanen-Sawatzky-Allen scheme,[64] in which the lowest-lying gap transition corresponds to the CT excitation from the O $2p$ to Mn $3d$ state and has four d electrons per Mn^{3+} site with a configuration of $t_{2g}^3 e_g^1$. This electronic configuration is susceptible to a strong electron-phonon coupling of the JT type that splits the e_g states into filled d_{z^2} and empty $d_{x^2-y^2}$ and, thus, produces large asymmetric oxygen displacements. Early theoretical work focused on the undistorted perovskite aristotype structure and it was found that usual LSDA cannot produce the correct insulating ground state for $LaMnO_3$.[29] Using the LAPW method, Pickett and Singh[39] obtained a gap of 0.12 eV for distorted $LaMnO_3$ when they include the JT effect and *A*-AF ordering. Our calculation also predicts insulating behavior in the *A*-AF phase of $LaMnO_3$ and it is discussed in detail below.

The valence-band DOS of $LaMnO_3$ are derived primarily from Mn $3d$ and O $2p$ admixture with dominant Mn $3d$ character (Fig. 5). From the projected density of states

(PDOS) it can be seen that the Mn $3d$–O $2p$ hybridization is spin dependent. For the case of the majority-spin channel both Mn $3d$ and O $2p$ strongly mix with each other in the whole VB. On the contrary, owing to the presence of Mn $3d$ in the high-spin state, the minority-spin VB is nearly empty for the Mn $3d$ states. Hence, there is little overlap between Mn $3d$ and O $2p$ states in the minority-spin channel. Because of CT from La and Mn to the O $2p$ states, the latter are almost filled and their contribution to the unoccupied state is minimal. The O $2s$ states are well localized and are present around -18 eV.

VB of *A*-AF phase of orthorhombic $LaMnO_3$ is generally composed of four regions. The lowest-energy region contains mainly O $2s$ bands; above this, the La $5p$ bands are distributed in the region between -17 eV and -14 eV. Both the O $2s$ and La $5p$ bands are well separated from the bands in the vicinity of E_F, and consequently they hardly contribute to the chemical bonding or to transport properties. The O $2p$ bands are present in the energy range -7 eV to -2 eV and energetically degenerate with the Mn $3d$ states in the whole VB region, indicating covalent interactions between Mn and O in $LaMnO_3$. The present observation of strong covalency in the ground state of $LaMnO_3$ is consistent with the conclusion drawn from photoemission and x-ray-absorption spectroscopy.[45] The negligible contribution of La electrons in the VB region indicates that there is an ionic interaction between La and the MnO_6 octahedra. It has been pointed out by Goodenough[65] that the covalency between the *A* site and oxygen is important for the $GdFeO_3$-type distortion. However, our PDOS profile shows that there is only a negligible amount of electrons present in VB from the *A* (La) site, indicating that the covalent interaction between La and O is rather unimportant in $LaMnO_3$. From PDOS along with the orbital-projected DOS we see that both Mn t_{2g} and e_g electrons participate in the covalent interaction with the neighboring oxygens. The top of VB is dominated by the majority-spin Mn $3d$ states, indicating the importance of Mn $3d$ states in transport properties such as CMR observed in hole-doped $LaMnO_3$. The bottom of the conduction band (CB) is dominated by the minority-spin Mn $3d$ electrons, and above the La $4f$ electrons are present in a very narrow energy range between 2.6 and 3.5 eV (Fig. 5). O $3d$ and Mn $4p$ states are found around 10 eV above E_F. As the Mn $3d$ states are playing an important role for the magnetism and other physical properties of $LaMnO_3$, it is worthwhile to investigate these in more detail.

An approximately cubic crystal field stemming from the oxygen octahedron around Mn would split the Mn $3d$ levels into t_{2g}-like and e_g-like levels. For Mn^{3+} in $LaMnO_3$, three electrons would occupy localized t_{2g} levels and one electron a linear combination of two e_g levels. The general view of the electronic structure of $LaMnO_3$ is that t_{2g} and e_g orbitals hybridize with O $2p$ orbitals, t_{2g} mainly with $2p$ π and e_g mainly with $2p$ σ. The t_{2g} electrons hybridize less with O $2p$ states and hence may be viewed as having local spins ($S=3/2$). In contrast to that, e_g orbitals, which hybridize more strongly, produce rather broad bands. The strong exchange interaction with the $t_{2g}^{\uparrow}$ subbands along with the JT

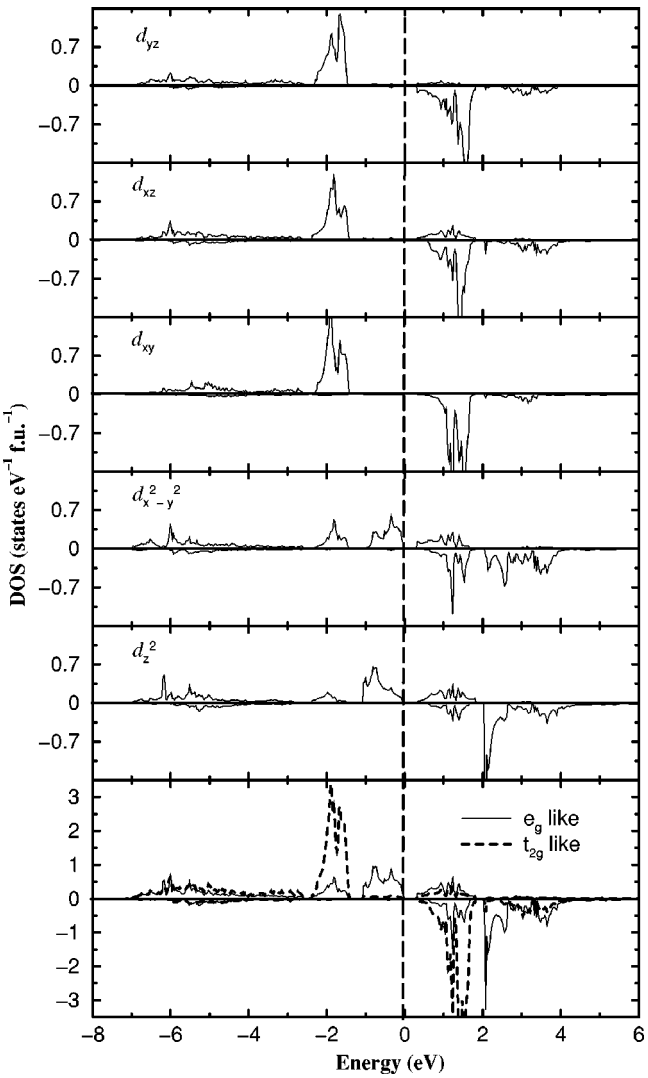

FIG. 6. Orbital-projected DOS for Mn in *A*-AF-state $LaMnO_3$ with orthorhombic $GdFeO_3$-type structure (results obtained from LAPW calculations).

distortion leads to the splitting of e_g into half-occupied $e_g^{\uparrow}$ and unoccupied $e_g^{\downarrow}$ bands (see Fig. 6). Our calculations show that t_{2g} bands form intense peaks in both VB and CB, and majority-spin t_{2g} bands are almost completely filled owing to the high-spin state of Mn in $LaMnO_3$. Due to the orthorhombic distortion, the orbital projected *d* DOS in Fig. 6 are significantly different from each other. Contrary to the general opinion, our orbital projected DOS's (Fig. 6) show that both e_g and t_{2g} electrons are present throughout the VB and hence both types of electrons participate in the covalent bonding with oxygen. Importantly, the JT distortion splits the e_g states in the *A*-AF orthorhombic phase and hence we find semiconducting behavior. Photoemission studies[45] show that the character of the band gap of $LaMnO_3$ is of the *p*-to-*d* CT type. Our site projected DOS predicts that there is considerable *p* and *d* character present at the top of the VB as well as in the low-energy region of the CB. A VB photoemission study[45] has been interpreted to suggest that the DOS closer to E_F in the VB contains contributions from Mn $e_g^{\uparrow}$. Our cal-

TABLE I. Total energy (relative to the lowest-energy state, in meV/f.u.) for $LaMnO_3$ in *A*-, *C*-, and *G*-AF, F, and P states with undistorted cubic (referred as cubic) and orthorhombic structures.

Method	*A*-AF	*C*-AF	G-AG	F	P	Reference
LSDA (LAPW)	0	52	42	18	—	47
LSDA (LMTO-ASA, cubic)	15	—	125	—	—	33
LSDA (LMTO-ASA)	15	—	110	0	—	33
LSDA+*U* (LMTO-ASA, cubic)	0	—	2042	1076	—	33
LSDA+*U* (LMTO-ASA)	0	—	204	34	—	33
GGA+SO (FLMTO)	0	66.5	60.4	24.7	1515.4	Present
GGA+SO (FLMTO, cubic)	406.9	439.4	573.1	347.5	1642.9	Present

culated orbital projected DOS in Fig. 6 is consistent with this photoemission study.

Owing to the JT distortion the e_g electrons are subjected to an OO effect in $LaMnO_3$. As the JT distortion influences the stability of the orbital configuration, one can expect that it also should affect the electronic structure of $LaMnO_3$ differently for different magnetic orderings. Hence, we next focus our attention on the electronic structure of orthorhombic $LaMnO_3$ in different magnetic configurations. The calculated total DOS for orthorhombic $LaMnO_3$ in the P, F, and *A*-, *C*-, and *G*-AF arrangements are shown in Fig. 4. From DOS at E_F in the P phase, one can deduce pertinent information concerning the magnetism in $LaMnO_3$. This shows that $LaMnO_3$ is a very favorable compound for cooperative magnetism since it has a large DOS value at E_F in the P state (Fig. 4). Owing to the splitting of e_g states by the JT distortion, a gap opens up at E_F in the DOS for the *A*-AF and *G*-AF phases (Fig. 4). It is interesting to note that the cubic phase of $LaMnO_3$ is always metallic irrespective of the magnetic ordering considered in the calculations. Thus the structural distortion is the key ingredient to account for the stabilization of the insulating behavior of $LaMnO_3$, consistent with earlier studies.[39] From Fig. 4 it is interesting to note that the P, F, and *C*-AF phases of $LaMnO_3$ are found to exhibit metallic conduction even when we include structural distortions in the calculation. This shows that apart from structural distortion, AF ordering also plays an important role for stabilizing the insulating behavior of $LaMnO_3$. Usually, the e_g splitting caused by the JT effect is somewhat underestimated in ASA calculations[27,29,30,34] and a discrepancy could reflect an uncertainty introduced by the ASA approach. The energy separation between the e_g and t_{2g} levels, caused by the crystal-field splitting, is known to be larger than 1 eV.[66] Our orbital-projected DOS yields a value of 1.1 eV between the t_{2g}- and e_g-like peak in Fig. 6. It should be noted that the e_g states are distributed in the whole VB even though their contribution is maximum near E_F. Owing to the well-separated e_g and t_{2g} levels in the cubic phase we estimated this energy to be ~ 0.96 eV. The JT distortion lifts the degeneracy of the e_g level. The e_g level splitting in our calculation is found to be 0.278 eV and this is nothing but the (semiconducting) band gap in this material. The Mn *d* exchange splitting obtained from our calculation is 3.34 eV and this is found to be in agreement with 3.5 eV found by Pickett and Singh[39] by a LAPW calculation and 3.48 eV reported by Mahadevan *et al.*[67] from LMTO-ASA calculations.

The LMTO-ASA (Ref. 33) calculations reveal that the splittings between the spin-up and spin-down states on introduction of the orthorhombic distortion are slightly asymmetric for the two types of Mn. However, our more accurate full potential calculations do not show any asymmetry of the splitting and the magnetic moments are completely canceled due to the AF interaction between the Mn ions. The total DOS in Fig. 4 show clearly that there is a gap opening near E_F in the *G*-AF phase with a value of 0.28 eV, comparable with that of the *A*-AF phase. As there is no band gap in the *C*-AF and F phases, the above results indicate that the AF coupling between the layers plays an important role in opening up the band gap in $LaMnO_3$. The DOS for the F phase shows a half-metallic feature; viz., there is a finite total DOS around E_F in one of the spin channels and a gap across E_F in the other spin channel. Owing to the F ordering within the ab plane in the *A*-AF phase and within ac in the *C*-AF phase, the DOS for these phases bears resemblance to that of the F phase. On the other hand, the DOS for the *G*-AF phase (dominated by the AF superexchange interactions) is quite different from that of the *A*-, *C*-AF, and F phases (Fig. 4). Moreover, in the *G*-AF phase the width of the e_g state is narrower than that in the *A*-, *C*-AF, and F phases and the partially filled e_g states in these phases are well separated from the empty t_{2g} states.

B. Magnetic properties

As the JT coupling between the e_g electrons and the distortion modes for the MnO_6 octahedra play an important role for the physical properties of $LaMnO_3$, a magnetic-property study of the undistorted cubic phase of $LaMnO_3$ is important. We have calculated the total energies and magnetic moments for $LaMnO_3$ in the undistorted cubic perovskite structure as well as for the orthorhombic structure with different magnetic configurations. The calculated total energies for the P, F, and *A*-, *C*-, and *G*-AF states of $LaMnO_3$ with the cubic perovskite structure relative to the *A*-AF phase with the orthorhombic structure is given in Table I. According to these data the cubic phase of $LaMnO_3$ should be stabilized in the F phase. Stabilization of the F phase in the cubic structure concurs with earlier findings.[33,39] The LAPW calculations of Hamada *et al.*[68] for undistorted $LaMnO_3$

show that the *A*-AF phase is 1 eV above the F phase, whereas Pickett and Singh[39] found a difference of only 110 meV. Our calculations show that the *A*-AF phase is 60 meV above the F phase in the cubic perovskite structure (Table I). We used the GGA, SO coupling, and a large number of **k** points along with a well-converged basis set. This may account for the difference between the present work and the earlier studies. Our orbital projected DOS for the *d* electrons of Mn (Fig. 2) show that the e_g electrons are only distributed in the vicinity of E_F in the majority-spin channel. The removal of the JT distortion enhances the exchange interaction originating from the e_g states drastically and also reduces the negative exchange from the t_{2g} state. Hence, the total interplane exchange interaction is positive and the system stabilizes in the F phase.

The calculated total energies of various magnetic configurations for $LaMnO_3$ in the orthorhombic structure (Table I) shows that the orthorhombic structure with *A*-AF ordering of the moments is the ground state for $LaMnO_3$. Stabilization of the *A*-AF state is consistent with the neutron-diffraction findings.[2,69] Further, our calculations predict that the F phase is only 24 meV higher in energy than the ground state. On the other hand, the P phase is ~ 1.4 eV higher in energy than the ground state. From the total energy of the various possible magnetic arrangements it is clear that intralayer exchange interactions in $LaMnO_3$ are F and considerably stronger than the AF interlayer couplings, the latter being very sensitive to lattice distortions. This observation is in agreement with the conclusion of Terakura *et al.*[70] from electronic structure studies and in qualitative agreement with inelastic neutron scattering results.[71,72] The present observation of a small energy difference between the *A*-AF and F phases is consistent with earlier theoretical studies.[73] It should be noted that LMTO-ASA calculations[33] predict the F state to be lower in energy than the AF state also for the orthorhombic structure (Table I). However, the LSDA+*U* calculations[33] with lattice distortion yielded the correct ground state. Hence, it has been suggested[33] that the correlation effect plays an important role for obtaining the correct electronic structure of $LaMnO_3$. It should also be noted that the theoretically optimized crystal-structure predicts[47] that F is more stable than the observed *A*-AF state. On the other hand, our calculations, without the inclusion of the correlation effect, give the correct ground state for $LaMnO_3$, indicating that the correlation effect after all may be less important.

If the interlayer F coupling is stronger than the intralayer AF coupling, the system will be stabilized in the *C*-AF phase. However, our calculations show that the *C*-AF phase is higher in energy than the *A*-AF and F phases. Due to the JT instability of Mn d^4, a substantial energy gain is expected when we include the actual structural distortions in our calculations. Hence, a gain of 0.323 eV/f.u. is found for F and 0.407 eV/f.u. for *A*-AF (Table I) when the structural distortions were included. The magnetic ordering is such that the difference in total energy between F and *A*-AF (*C*-AF) gives information about the exchange-coupling energy within the plane (perpendicular to the plane for *C*-AF). Our calculations show that the AF intraplane exchange interaction energy is smaller (24 meV for the orthorhombic phase and 59 meV for the cubic phase) than the AF interplane exchange interaction energy (41 meV for the orthorhombic phase and 92 meV for the cubic phase). The present findings are consistent with the experimental studies in the sense that neutron scattering measurements[71] on a $LaMnO_3$ single crystal showed a strong intraplane F coupling and a weak AF interplane coupling.

Now we will try to understand the microscopic origin for the stabilization of *A*-AF in $LaMnO_3$. In the ideal cubic lattice the hybridization between the Mn t_{2g} and e_g states is nearly vanishing. As expected for a half-filled t_{2g} band, the t_{2g}-type interatomic exchange facilitates AF ordering. Our orbital-projected DOS show that the d_{z^2} and $d_{x^2-y^2}$ electrons are distributed in the whole VB region and are mainly populated at the top of the VB. The JT distortion induces orbital ordering in which the orbitals confined to the *ab* plane ($d_{x^2-r^2}$ and $d_{y^2-r^2}$) are dominantly populated and the counter e_g orbitals of d_{z^2} symmetry are less populated in the vicinity of E_F. In this case itinerant band ferromagnetism is operational in the *ab* plane and is responsible for the F ordering within the plane. The electrons in the d_{yz} and d_{xz} orbitals are well localized and these make the interplane exchange interaction AF, which in turn stabilizes the *A*-AF phase. Further, the localized nature of the electrons in the d_{xy} orbital enhances the AF coupling within the layers and in turn makes the energy difference between the F and *A*-AF phases very small. The CMR effect in manganites may be understood as follows. When charges are localized by strong electron-electron interactions the system becomes an AF insulator, but this state is energetically very close to the metallic F state in $LaMnO_3$. Consequently, aligning of spins with an external magnetic field will activate metallic F states and cause a large gain of kinetic energy, i.e., a CMR phenomenon.

In order to understand the role of structural distortion for the stabilization of the magnetic structure of $LaMnO_3$ we have made two sets of additional calculations, one involving only the rotation of the octahedra without JT distortion and the other involving only the JT distortion without rotation of the octahedra. If we include JT distortion alone in our calculation the *A*-AF state is around 6 meV lower in energy than the F solution. In contrast, the calculation which involves rotation of the octahedra alone yields the F state to be stable with 53 meV lower energy than the *A*-AF state. These calculations suggests that JT distortion plays an important role in the stabilization of *A*-AF in $LaMnO_3$.

Table II lists the calculated magnetic moment at the Mn site in $LaMnO_3$ for different spin configurations in the undistorted cubic perovskite structure as well as the distorted orthorhombic structure, including for comparison corresponding values from other theoretical studies and experimental neutron-diffraction results. Without hybridization, the Mn spin moment should take an appropriate integer value (4 μ_B/Mn atom in the case of the high-spin state) and the moment on oxygen should be negligible. Owing to the covalent interaction between the Mn *d* and O *p* states, experimental as well as theoretical studies will give smaller Mn moments than predicted by the ionic model. For the F phase in the orthorhombic structure, Mn polarizes the neighboring oxy-

TABLE II. Calculated magnetic moment (in μ_B/Mn atom) for $LaMnO_3$ in AF (*A*-, *C*-, *G*-type) and F states. The total moment (total) refers to one formula unit.

Method	*A*	*C*	*G*	F	F, total	Reference
LSDA (LMTO-ASA, cubic)	3.81	—	3.64	3.81	—	33
LSDA (LMTO-ASA)	3.73	—	3.63	3.76	—	33
LSDA+*U* (LMTO-ASA)	3.72	—	3.63	3.76	—	33
GGA+SO (FLMTO)	3.433	3.356	3.272	3.509	3.976	Present
GGA+SO (FLMTO, cubic)	3.315	3.278	3.134	3.318	3.698	Present
GGA (FLAPW)	3.394	—	—	3.295	3.525	Present
Experiment	3.7 ± 0.1					49
Experiment	3.42					74

gens and the induced moment at the O(1) site is $0.07\mu_B$/atom and at the O(2) $0.059\mu_B$/atom and these moments are coupled ferromagnetically with the local moments of Mn^{3+}. There are small differences in the magnetic moments for the different magnetic arrangements, indicating that these moments have a distinct atomic-like character. From Table II it should be noted that the LMTO-ASA approach generally gives larger moments than the accurate full-potential calculation. The reason for this difference is that the full-potential calculations estimate the moments using only the spin density within the muffin-tin spheres so that the spin density in the interstitial region is neglected. Our calculated magnetic moment at the Mn site in the *A*-AF orthorhombic structure is found to be in excellent agreement with the neutron-diffraction measurement[74] on well-characterized samples (Table II).

The electric field gradient for Mn in the F phase obtained by the FLAPW calculation is 3.579×10^{21} V/m^2 as compared with -1.587×10^{21} V/m^2 for the *A*-AF phase. The asymmetry parameter η of the electric field gradient tensor follows from the relation $\eta=(V_{xx}-V_{yy})/V_{zz}$, which gives $\eta=0.95$ for Mn in the *A*-AF phase in good agreement with $\eta=0.82$ obtained from low-temperature perturbed-angular-correlation spectroscopy.[75] The magnetic hyperfine field at the Mn site derived from our FLAPW calculation is 198 kG for the *A*-AF phase and 176 kG for the F phase.

A comment on the appearance of the F state by doping of divalent elements in $LaMnO_3$ is appropriate. It has long been believed that the appearance of the F ground state in metallic $La_{1-x}A_xMnO_3$ can be explained by the double-exchange interaction of Mn^{3+} ($t_{2g}^3e_g^1$) and Mn^{4+} ($t_{2g}^3e_g^0$). Recent experiments and theoretical investigations have revealed many discrepancies in the simple double-exchange model. Urushbara *et al.*[76] pointed out that the simple double-exchange model is methodologically inappropriate for predicting the AF insulating phase ($0.1\leqslant x\leqslant0.15$, $T<T_C$), as well as for the canted AF insulating phase with large canting angle or large magnetic moments (as estimated by Kawano *et al.*[77] in the F phase region). Millis *et al.*[19] proposed that in addition to the double-exchange mechanism, a strong electron-phonon interaction arising from the JT splitting of the outer Mn *d* level is important. As our calculations predict the cubic phase of $LaMnO_3$ to take the F state, there must be another mechanism than doping by divalent elements which reduces the JT distortion and in turn increases the interlayer exchange coupling to stabilize the F state. Moreover, our calculations show that within the *ab* plane the Mn ions are F coupled without involvement of Mn in different ionic states. If the double-exchange mechanism is operational in $LaMnO_3$, one can expect a charge imbalance between the Mn atoms in the *ab* plane (with F alignment). This suggests that the F coupling in $LaMnO_3$ can be explained within the framework of itinerant-band ferromagnetism.

C. Magneto-optical properties

The magneto-optical Kerr effect (MOKE) can be described by the off-diagonal elements of the dielectric tensor which in a given frequency region originates from optical transitions with different frequency dependence for right (RCP) and left (LCP) circularly polarized light caused by the SO splitting of the states involved.[78] Considerable interest has recently been focused on studying the MO properties of materials owing to their potential for applications in rewritable high-density data storage. For magneto-optical information storage one requires materials with a large Kerr effect as well as perpendicular magnetic anisotropy. Uniaxial magnetic anisotropy is observed for $La_{0.67}Ca_{0.33}MnO_3$ films grown on $SrTiO_3$ [001] substrates[79] and confirmed theoretically.[80]

The energy difference between the *A*-AF and F states of $LaMnO_3$ is very small and hence a small magnetic field could drive a transition from *A*-AF to F. Also, it is interesting to note that $LaMnO_3$ produced by annealing in an oxygen atmosphere shows[81] a simple F structure below $T_C=140$ K, with moments oriented along *c*. Manganites exhibiting the CMR effect are also in the F state and hence it is interesting to study the F phase of $LaMnO_3$ in more detail. Polar Kerr rotation measurements on hole doped $LaMnO_3$ show that Bi doping enhances the Kerr rotation to a value of 2.3° at 78 K and a wavelength of 0.29 nm.[82] It may be recalled that the large MO effect in MnPtSb is usually linked with its half-metallic behavior.[83] Hence, as the F phase of $LaMnO_3$ also possesses half-metallic behavior with a band gap of 2.38 eV (between the top of the minority-spin VB and the bottom of the CB in Fig. 4), it is interesting to examine its MO properties.

In the case of F-state $LaMnO_3$, our calculations predicted half-metallic behavior and hence the intraband contribution will be of importance to predict the MO property reliably. Therefore, we have taken into account the intraband contribution using the Drude formula with the same relaxation time as earlier.[84] We have calculated the unscreened plasma frequency by integrating over the Fermi surface using the FLAPW method. For F-state $La_{0.7}Ca_{0.3}MnO_3$, Pickett and Singh predicted[85] a plasma frequency corresponding to 1.9 eV. Several groups have reported an anomalously small Drude weight in both $La_{0.7}Ca_{0.3}MnO_3$ and $La_{0.7}Sr_{0.3}MnO_3$.[66,86] Interpreting the latter findings in terms of enhanced optical mass, the effective mass values established optically are much greater than those derived from the specific-heat measurements.[87] The theoretically established half-metallic feature of the F state in $LaMnO_3$ suggests that the small Drude weight is originating from large exchange splitting which contracts the Drude contribution coming from the minority-spin channel. In accordance with the half-metallic nature of the F state, our calculated DOS at E_F is small [3.36 states/(Ry f.u.)] As a result, the calculated unscreened plasma frequency along *a*, *b*, and *c* corresponds to 1.079, 1.276, and 0.926 eV, respectively. Owing to the half-metallic nature of this material, there is no intraband contribution arising from the majority-spin channel. Hence, we conclude that the experimentally observed[66,86] anomalously small Drude weight in $La_{0.7}Ca_{0.3}MnO_3$ and $La_{0.7}Sr_{0.3}MnO_3$ is due to half-metallic behavior. Our calculated MO spectra for F-state $LaMnO_3$ are given in Fig. 7. Our recent MOKE studies[88] of FePt shows that Kerr rotation spectra can be reliably predicted even up to as high energies as 10 eV with the formalism adopted here. Hence, we have depicted the calculated MO spectra up to 8 eV in Fig. 7. The Kerr rotation (θ_K) shows a positive or negative peak when the Kerr ellipticity (η_K) passes through zero. The frequency-dependent Kerr-rotation and -ellipticity spectra are experimentally established[82,89] for hole-doped $LaMnO_3$. As there are no experimental MO spectra available for comparison with our theoretical spectra for (pure) F-state $LaMnO_3$, we have made a comparison with the experimetal spectrum for hole-doped $LaMnO_3$ (Fig. 7).

MO effects are proportional to the product of the SO-coupling strength and the net electron-spin polarization. This makes MO effects sensitive to the magnetic electrons, i.e., to the $3d$ electrons of Mn in $LaMnO_3$. In order to promote understanding of the microscopic origin of the MO effect, we present the off-diagonal elements of the imaginary part of the dielectric tensor in Fig. 8. Note that ϵ_2^{xy} can have either positive or negative sign since it is proportional to the difference in the absorption of RCP and LCP light. The sign of ϵ_2^{xy} is thus directly related to the spin polarization of the electronic states that contributes to the MO effect. Owing to the half-metallic behavior of the F state of $LaMnO_3$, the off-diagonal components of the dielectric tensor below 2.46 eV originate only from the majority-spin electrons (see Fig. 8). So the peaks at 0.4, 0.9, and 2 eV in the Kerr rotation spectra stem from the transition from the Mn $e_g^{\uparrow}t_{2g}^{\uparrow}$ to the hybridized Mn-O $\mathrm{Mn}(e_g t_{2g} - \mathrm{O}2p)^{\uparrow}$ bands. The experimental ϵ_2^{xy} spectra show[89] two peaks, one at 1.2 eV and the other at 3.5 eV. These are assigned to involve transitions of minority spin electrons: $t_{2g}^3 e_g^1 \rightarrow t_{2g}^3 e_g^2 L$ and $t_{2g}^3 e_g^1 \rightarrow t_{2g}^4 e_g^1 L$, respectively. The absence of the 3.5 eV peak in the theoretical spectra indicates that it is an effect of the hole doping.

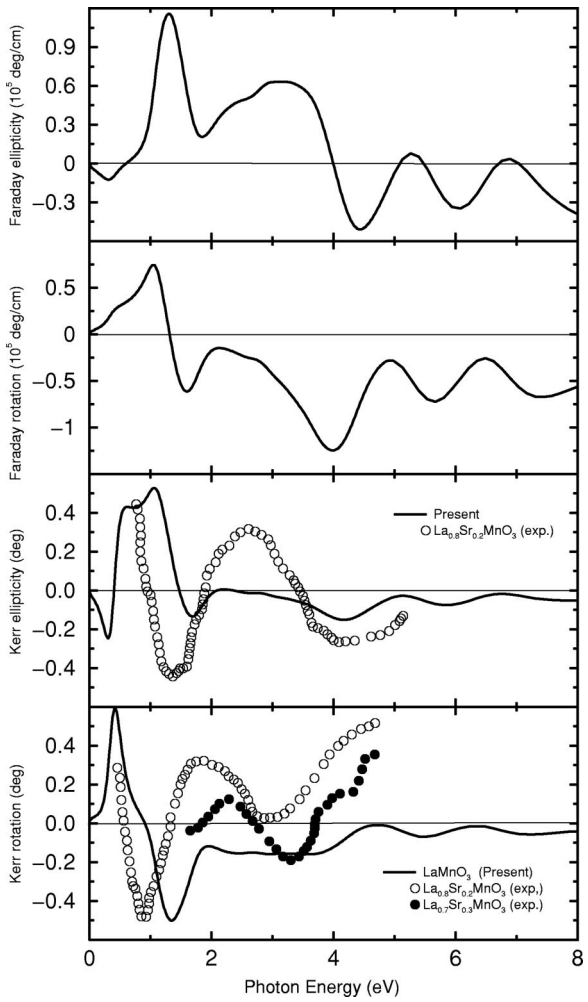

FIG. 7. Magneto-optical Kerr rotation, ellipticity, Faraday rotation, and ellipticity spectra obtained for F-state $LaMnO_3$ with the orthorhombic $GdFeO_3$-type structure. The experimental Kerr rotation spectrum for $La_{0.7}Sr_{0.3}MnO_3$ is taken from Ref. 82 and the experimental Kerr rotation and Kerr ellipticity spectra for $La_{0.8}Sr_{0.2}MnO_3$ are taken from Ref. 89.

It is experimentally observed that Kerr rotation spectra change significantly with the temperature[82] as well as with the doping level.[89] Our calculated MO spectra are valid only for stoichiometric F-state $LaMnO_3$ at low temperature. The polar MO Kerr rotation data for $La_{0.7}Sr_{0.3}MnO_3$ at 78 K were taken from the experimental spectra of Popma and Kamminga.[82] Even though the experimental MO spectrum for $La_{0.8}Sr_{0.2}MnO_3$ was measured[89] at 300 K with a magnetic field of 2.2 kOe, our calculated Kerr rotation spectrum is comparable in the lower-energy region (Fig. 7). The discrepancy between the experimental and theoretical Kerr spectra in the higher-energy region may be explained as a temperature and/or hole doping effect. We hope that our theoretical findings may motivate measurements on fully magnetized

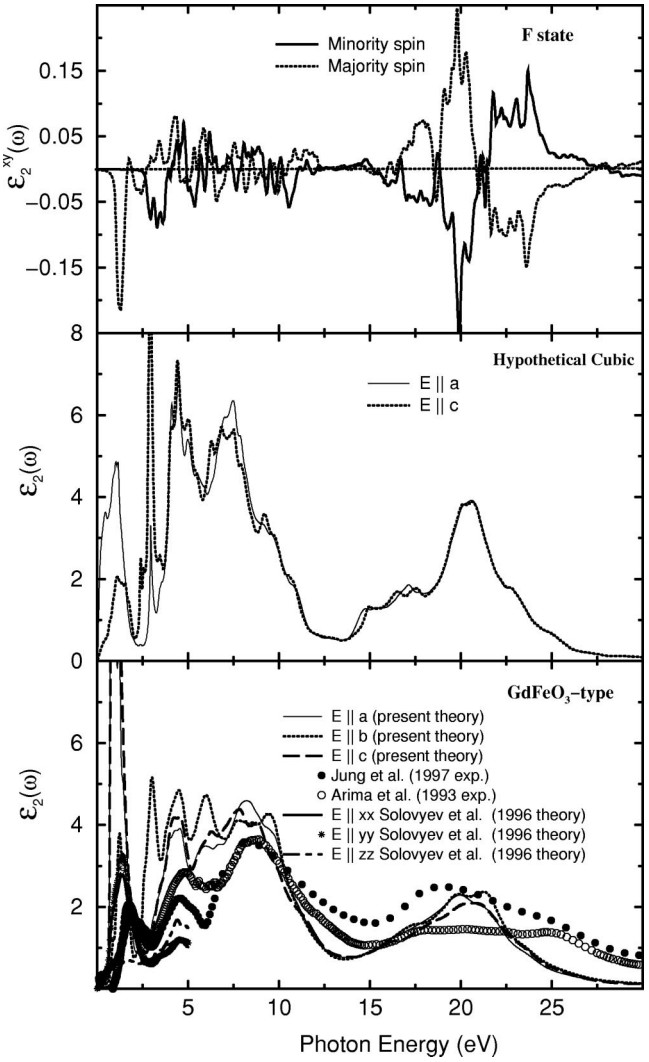

FIG. 8. Imaginary part of optical dielectric tensors for the diagonal elements $[\epsilon_2(\omega)]$ for *A*-AF-state $LaMnO_3$ in hypothetical cubic and real orthorhombic $GdFeO_3$-type structures. Off-diagonal element for the imaginary part of the dielectric tensor $[\epsilon_2^{xy}(\omega)]$ for F-state $LaMnO_3$ with the $GdFeO_3$-type orthorhombic structure. The experimental $\epsilon_2(\omega)$ data are taken from Refs. 91 and 63 and the theoretical data are from Ref. 27.

$LaMnO_3$ at low temperatures. Solovyev[90] has performed theoretical calculations on MO properties such as Kerr rotation and ellipticity for $LaMnO_3$ for different canted-spin configurations. As the F state is only 24 meV above the ground state, it is quite possible that the F state can be stabilized experimentally. However, since we have studied the MO properties of F-state $LaMnO_3$, our result cannot be compared with the findings of Solovyev.[90]

Lawler *et al.*[28] found strong Faraday rotation at 1.5 eV ($\theta_F > 1\times10^4$ deg/cm) and 3 eV ($\theta_F > 4\times10^4$ deg/cm) for $La_{1-x}Ca_xMnO_3$ ($0.2 \leqslant x \leqslant 0.5$). Our theoretical Faraday rotation spectra also show two prominent peaks at 1.5 and 4 eV, the latter having the highest value ($\sim 1.25\times10^5$ deg/cm) in the spectrum. The lower-energy peak in the experimental spectrum[28] of $La_{1-x}Ca_xMnO_3$ is interpreted as associated with both ligand-to-metal charge transfer and *d*-*d* transitions.

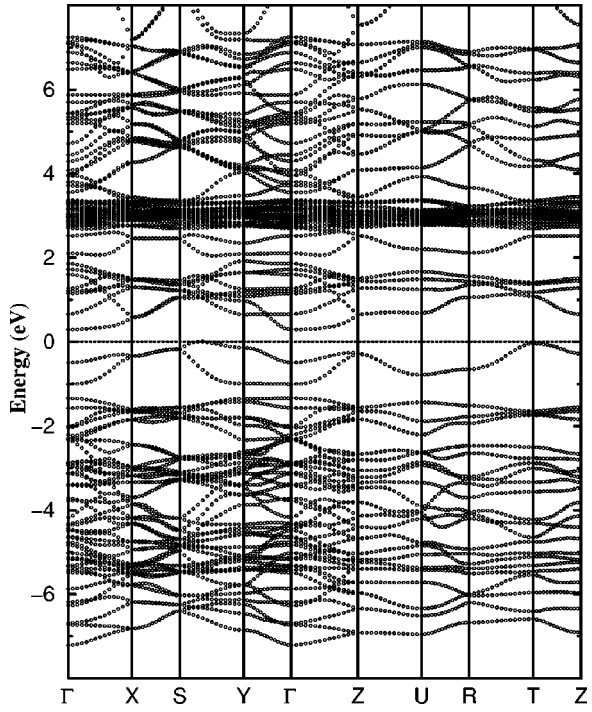

FIG. 9. Calculated electronic energy-band structure for *A*-AF-state $LaMnO_3$ in orthorhombic $GdFeO_3$-type structure. Fermi level is set at zero. Relevant symmetry directions in the Brillouin zone are indicated.

However, there are as yet no experimental frequency-dependent Faraday rotation and ellipticity measurements available.

D. Optical properties

A deeper understanding of optical properties is important from a fundamental point of view, since the optical characteristics involve not only the occupied and unoccupied parts of the electronic structure but also the character of the bands. So in order to compare the band structure of $LaMnO_3$ directly with experimental facts[63,91,92] we have calculated the optical spectra for $LaMnO_3$ (for earlier theoretical studies see Refs. 27 and 46). The experimental reflectivity spectra are rather confusing and controversial (see the discussion in Ref. 92). Recent experiments[92] indicate that the optical spectrum of the manganites is very sensitive to the condition at the surface. As the optical properties of materials originate from interband transitions from occupied to unoccupied bands it is more instructive to turn to the electronic energy-band structure. The calculated energy-band structure of $LaMnO_3$ in the *A*-AF-state orthorhombic structure is shown in Fig. 9. From this illustration it is immediately clear that $LaMnO_3$ is an indirect band-gap semiconductor where the band gap is between the S-Y direction on the top of the VB and the Γ point at the bottom of the CB. There are two energy bands present at the top of the VB, well separated from the rest of the VB. Our detailed analysis shows that these two energy bands have mainly Mn $d_{x^2-y^2}$ and d_{xz} character with a small contribution from O *p*. The La $4f$ electrons contribute with a cluster of bands between 2.5 and 3.5

eV in the CB (Fig. 9). The Mn $3d$ and O $2p$ electrons are distributed over the whole energy range of the VB.

Saitoh *et al.*[45] reported strong covalency and suggested that the energy gap in $LaMnO_3$ should be considered as of the CT type. The band gap estimated from our DOS studies for *A*-AF-state $LaMnO_3$ is 0.278 eV and this is found to be in good agreement with the value of 0.24 eV obtained from resistivity measurements by Mahendiran *et al.*[93] whereas Jonker[94] reported 0.15 eV. However, our value for the direct gap (0.677 eV) between occupied and empty states at the same location in BZ is too low in comparison with optical [1.1 eV (Ref. 63)] and photoemission [1.7 eV (Ref. 45)] measurements. (It should be noted, however, that optical gaps are usually defined at the onset of an increase in spectral intensity in the measured optical variable.) It is also useful to compare our calculated band gap with other theoretical results. The LSDA and LSDA+U calculations of Yang *et al.*[95] using the LMTO-ASA method gave a band gap of 0.1 and 1.0 eV, respectively. The LSDA+$U2$ approach[27] (where U is applied only to the t_{2g} electrons) yielded a band gap of 0.2 eV. Hence, our band gap is somewhat larger than that of other LSDA calculations. On the other hand, Hartree Fock calculations[96] gave an unphysically large gap (3 eV) for $LaMnO_3$.

As all the linear optical properties can be derived from $\epsilon_2(\omega)$ we have illustrated this quantity in Fig. 8 and we have compared our theoretical spectra with the experimental $\epsilon_2(\omega)$ spectra derived from reflectivity measurements. The illustration shows that our calculated spectra are in good agreement with the experimental data at least up to 20 eV. This indicates that unlike earlier reported ϵ_2 spectra (obtained from ASA calculations[27,46]) accurate full-potential calculations are able to predict the electronic structure of $LaMnO_3$ reliably, not only for the occupied states, but also for the excited states. It is interesting to note that we are able to predict correctly the peaks around 1.5, 4.7, 8.8, and 20 eV without the introduction of so-called scissor operations. This suggests that electron-correlation effects are less significant in $LaMnO_3$. The peak around 4.7 eV is reasonably close to the experimental feature reported by Arima *et al.*[63] (Fig. 8). Our theoretical peak at 8.8 eV is in quantitative agreement with both sets of experimental data included in the figure. Our calculations are also able to predict correctly the experimentally observed peak at 20 eV by Jung *et al.*[91] (which Arima *et al.*[63] failed to record).

Now we will try to understand the microscopic origin of the optical interband transitions in $LaMnO_3$. The peak around 1.5 eV has been assigned[91] as intra-atomic $e_g^1(Mn^{3+}) \rightarrow e_g^2(Mn^{3+})$ transitions. Note that such $d \rightarrow d$ transitions are not allowed by the electric dipole selection rule, but it has been suggested[97] that a strong hybridization of the e_g bands with the O $2p$ bands will make such $d \rightarrow d$ transitions optically active. The interband transition between JT-split bands gives low-energy transitions in the $\epsilon_2(\omega)$ spectra and the sharp peak features present in $\epsilon_2 \| a$ and $\epsilon_2 \| c$ are attributed to such interband transitions. The partial DOS for $LaMnO_3$ given in Fig. 5 show that there is a considerable amount of O $2p$ states present at the top of the VB as well as at the bottom of the CB arising from strong covalent interactions between Mn d and O p states. Hence, we propose that the lower-energy peak in the $\epsilon_2(\omega)$ spectra originates from [(Mn $d_{x^2-y^2}$ d_{xz};O p hybridized)$\rightarrow$(Mn d;O p)] optical interband transitions. The peak around 4.7 eV in the $E \| b$ $\epsilon_2(\omega)$ spectrum originates mainly from hybridized (Mn d_{z^2},O p) states to unoccupied hybridized (Mn $3d$;O p) states. All the majority-spin d electrons participate in the interband transition from 3 up to 10 eV (Fig. 8).

In the cubic case $\epsilon_2(\omega)$ is a scalar, and in the orthorhombic case it is a tensor. So we have calculated the dielectric component with the light polarized along a, b, and c as shown in Fig. 8. The optical anisotropy in this material can be understood from our directional-dependent, optical dielectric tensor shown in Fig. 8. From the calculations we see that the $\epsilon_2(\omega)$ spectra along a and c are almost the same. Large anisotropy is present in the lower-energy region of the $\epsilon_2(\omega)$ spectra. In particular sharp peaks are present for $E \| a$ and $E \| c$ which are less pronounced for $E \| b$. The optical conductivity obtained by Ahn and Millis[26] from tight-binding parametrization of the band structure also shows a sharp peak feature in the lowest-energy part of σ_{xx} whereas this feature is absent in the σ_{zz} spectrum. Our calculation predicts that the interband transition due to JT splitting is less pronounced in the ϵ_2 spectrum corresponding to $E \| b$. In order to confirm these theoretical predictions polarized optical-property measurements on $LaMnO_3$ are needed.

Solovyev[98] suggested that the optical anisotropy in *A*-AF-state $LaMnO_3$ is due to two factors: (i) Owing to large exchange, splitting the minority-spin d_{z^2} states near E_F will contribute less to ϵ_2^{xx}. (ii) Owing to *A*-AF ordering and JT distortion, the contribution of d_{z^2} character to the states with d_{x^2} and d_{z^2} symmetry is significantly reduced and hence the intensity of ϵ_2^{xx} in the low-energy region should also be reduced. In order to understand the role of JT distortion for the optical properties of $LaMnO_3$, we calculated also the optical dielectric tensor for $LaMnO_3$ in the cubic perovskite structure with *A*-AF ordering (Fig. 8). Just like for the orthorhombic *A*-AF phase, there is large optical anisotropy present in the lower-energy (<2 eV) part of the spectrum. This indicates that the *A*-AF spin ordering is responsible for the large anisotropy in the optical dielectric tensor which in turn is a result of different spin-selection rules applicable to in-plane and out-of-plane optical transitions. However, the optical anisotropy in the orthorhombic *A*-AF phase is much larger than that in the corresponding undistorted cubic phase (Fig. 8), indicating that apart from *A*-AF ordering, JT distortion also contributes to the large optical anisotropy in the lower-energy region of the optical spectra of $LaMnO_3$.

In order to compare our calculated spectra with those obtained by the LMTO-ASA method, we have plotted the optical dielectric tensors obtained by Solovyev *et al.*[27] from the LSDA calculations in Fig. 8. Our calculated $E \| b$ spectrum below 2 eV is found to be in good agreement with the $E \| xx$ and $E \| yy$ spectra of these authors. However, their $E \| zz$ spectrum is much smaller in the lower-energy region than our results as well as the experimental findings (Fig. 8). From the optical spectrum calculated by the LDA+U method, Solovyev *et al.*[27] found that the low-energy part (up

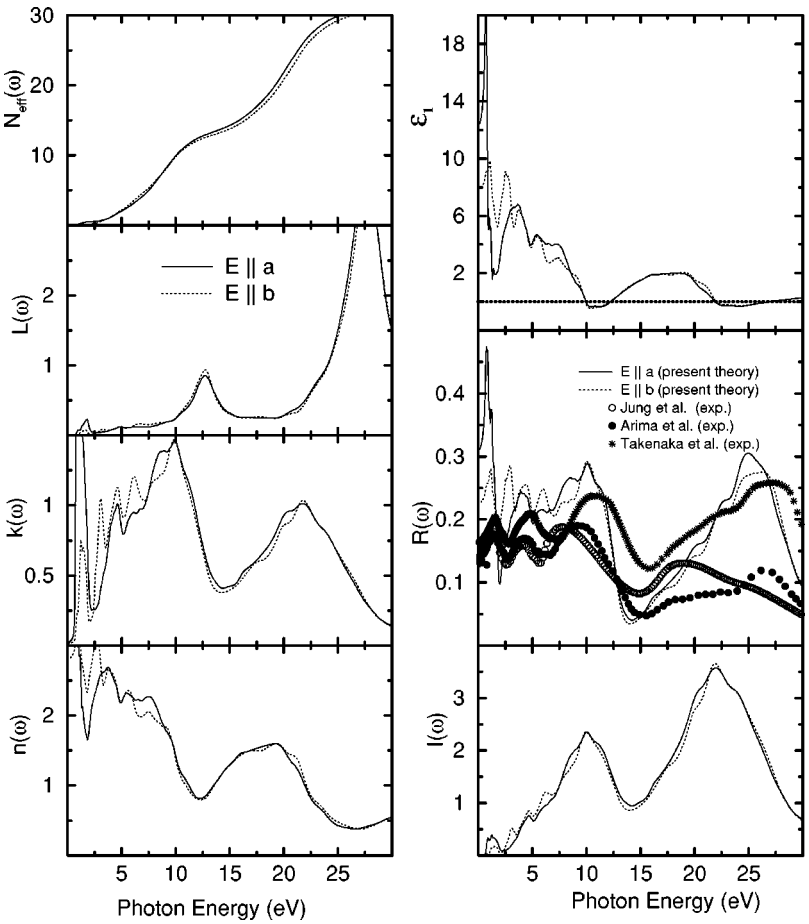

FIG. 10. Calculated linear optical properties; absorption coefficient $[\mathrm{I}(\omega)$ in 10^5 $\mathrm{cm}^{-1}]$, reflectivity $[\mathrm{R}(\omega)]$, real part of optical dielectric tensor $[\epsilon_1(\omega)]$, refractive index $[n(\omega)]$, extinction coefficient $[k(\omega)]$, electron energy loss function $[L(\omega)]$, and effective number of electrons participating the optical interband transition $[N_{eff}(\omega)$ in electrons/f.u.] for *A*-AF-state $LaMnO_3$ with $GdFeO_3$-type orthorhombic structure. The experimental reflectivity spectra are taken from Refs. 63, 91, and 99.

to 3 eV) reflects excitations from O *p* to an unoccupied band formed by alternating Mn $d_{x^2-z^2}$ and $d_{y^2-z^2}$ orbitals. However, their study poorly described the higher-energy excitations. This discrepancy may be due to the limitations of the ASA or the minimal basis they have used in the calculation (La $4f$ states were not included). Bouarab *et al.*[46] calculated optical conductivity spectra for $LaMnO_3$. They used the LMTO-ASA method where nonspherical contributions to the potential are not included. Further, these calculations were made with a minimal basis set for the undistorted cubic perovskite structure rather than the actual distorted perovskite structure. Hence, it does not make sense to compare our calculated optical spectra directly with the latter findings.

As the linear optical spectra are directly measurable experimentally, we have reported our calculated optical spectra in Fig. 10. Also, to understand the anisotropy in the optical properties of $LaMnO_3$ we show the linear optical spectra for $LaMnO_3$ along the *a* and *b* axes in the same illustration. A large anisotropy in the optical properties for the low-energy region is clearly visible in the reflectivity as well as the extinction coefficient spectra. (Figure 10 shows the experimentally measured reflectivity by Jung *et al.*,[91] Arima *et al.*,[63] and Takenaka *et al.*[99] in comparision with calculated spectra from our optical dielectric tensors.) The reflectivity measured by Takenaka *et al.*[99] above 8.4 eV is found at a higher value than found in the spectra of two other experiments[63,91] (Fig. 10). Overall our calculated reflectivity spectra are found to be in good qualitative agreement with the experimental spectra up to 30 eV (Fig. 10). The peaks around 10 and 25 eV in our reflectivity spectra concur with the findings of Takenaka *et al.*[99] As the optical properties of $LaMnO_3$ are anisotropic, it is particularly interesting to calculate the effective number of valence electrons, $N_{eff}(\omega)$, participating in the optical transitions in each direction. Hence, we have calculated (see Ref. 84) the number of electrons participating in the optical interband transitions in different crystallographic directions, and the comparison between $N_{eff}(\omega)$ for the $E\|a$ and $E\|b$ spectra shows significant differences in the low-energy region (Fig. 10). Except for the reflectivity, there is no optical properties measurements for $LaMnO_3$ available. Hopefully our findings will motivate such studies.

E. XPS and BIS studies

In spite of intense experimental[43–45,91,100] and theoretical[27,34,39,41] efforts to understand the electronic structure of $LaMnO_3$, there are still a number of ambiguities concerning the VB features. Both x-ray photoemission spectroscopic (XPS) and ultraviolet photoemission spectroscopic (UPS) experiments showed a double-peak structure between -10 eV and E_F.[44,45,100] Even though it is widely accepted that the double-peak structure arises from O *p* and Mn *d* bands, an important controversy still remains in that some authors[34,41,45] have argued that the O *p* band lies below the Mn t_{2g} bands, while others[91] have suggested the opposite. In Fig. 11 we have compared our calculated value of the VB

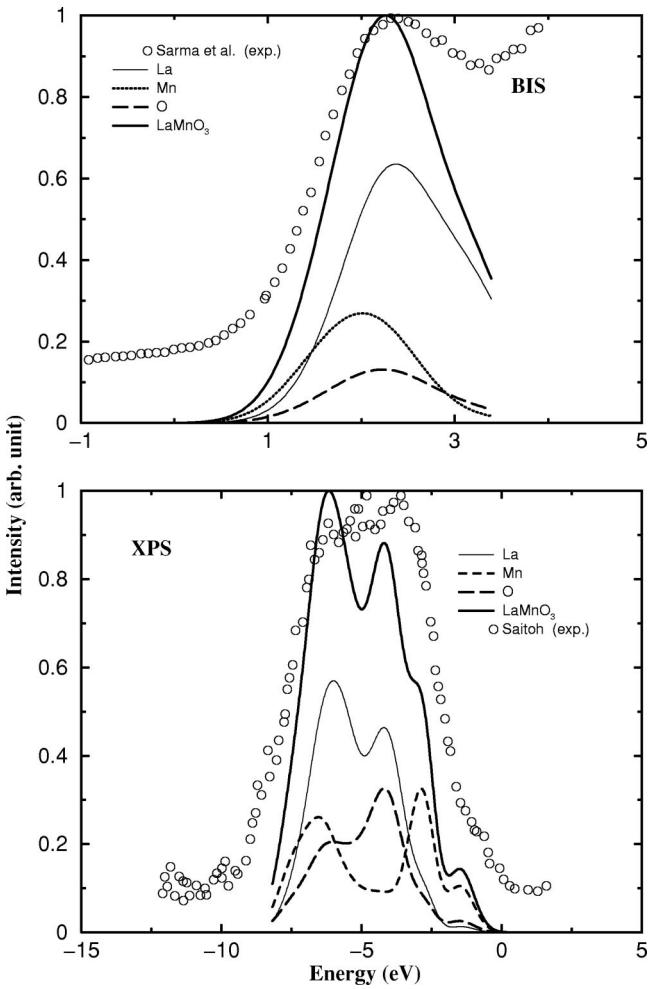

FIG. 11. XPS and BIS spectra for *A*-AF-state $LaMnO_3$ with $GdFeO_3$-type orthorhombic structure. Experimental XPS spectrum is taken from Ref. 45 and BIS spectrum from Ref. 41.

XPS intensity with the experimental spectra.[45] In all the experimental studies, the main VB features have a marked increase in binding energy around 1.5–2 eV, remaining large in the region 2–6 eV, and falling off in the range 6–8 eV.

The experimental XPS data show three peak features between -7 and -3 eV. As can be seen from Fig. 11, these three peaks are well reproduced in the calculated profile. The large experimental background intensity makes a direct comparison with the calculated peak feature around -1.8 eV difficult. The overall agreement between the theoretical and experimental positions of peaks and shoulders in the XPS spectra is very satisfactory (Fig. 11). Note that the experimental XPS spectra do not exhibit any appreciable intensity in a correlation-induced satellite at higher binding energies in contrast to the intense satellite features usually found in transition-metal monoxides, e.g., NiO. Thus, the good agreement between experimental and theoretical spectra indicates that the on-site Coulomb correlation effect is not significant in $LaMnO_3$.

Knowledge of the theoretically calculated photoemission spectra (PES) has the advantage that one can identify contributions from different constituents to the PES intensity in different energy ranges. From Fig. 11 it is clear that the XPS intensity in the energy range -3.5 eV to E_F mainly originates from Mn *d* states. The O *p* electrons contribute to the PES intensity in the energy range -7–3.5 eV. Below -4 eV both La and Mn atoms contribute equally to the PES intensity. Pickett and Singh[39] compared their theoretical DOS with PES and found significant differences. Thus, the good agreement between the experimental and our theoretical XPS indicates that the matrix-element effect is important in $LaMnO_3$.

We now turn to a discussion of the BIS spectra. The physical process in BIS is as follows. An electron of energy E_1 is slowed down to a lower-energy level E_2 corresponding to an unoccupied valence state of the crystal. The energy difference is emitted as bremsstrahlung radiation, which reflects the density of unoccupied valence states.[101] Our calculated BIS spectrum is compared with the experimental spectrum[38] in Fig. 11 which show that theory is able to reproduce the experimentally observed peak at 2 eV. There is an intense peak above 3.5 eV in the experimental spectrum which originates from the La $4f$ electrons, but owing to its large intensity, this is not shown in Fig. 11.

F. XANES spectra

Another experimental technique that provides information about CB is x-ray absorption spectroscopy. Calculated O $K\alpha$, Mn $K\alpha$, and Mn $L_{II,III}$ XANES spectra for $LaMnO_3$ are shown in Fig. 12. Because of the angular momentum selection rule (dipole approximation), only O $2p$ states and Mn $4p$ states contribute to the O *K*-edge and Mn *K*-edge spectra, respectively. The Mn $4s$ and Mn $3d$ states contribute to the Mn $L_{II,III}$ spectrum. The calculated XANES spectrum for the O *K* edge (VB$\rightarrow 1s$) is given in the upper panel of Fig. 12 along with available experimental data.[44,102] The experimental spectrum has two prominent peaks in the low-energy range and both are well reproduced in our theoretical spectra even without including the core-hole effect in the calculations. As reflected in different Mn-O distances there are two kinds (crystallographically) of oxygens present in $LaMnO_3$ and these have considerable different peak positions in the XANES spectra.

The calculated $L_{II,III}$ spectrum is shown in the middle panel of Fig. 12. Owing to the nonavailability of experimental Mn $L_{II,III}$ spectra for $LaMnO_3$, we have compared our calculated spectrum with that experimentally established[103] for Mn^{3+} in Mn_2O_3. The calculated Mn *K*-edge spectrum for $LaMnO_3$ is given in the lower panel of Fig. 12 along with the available experimental *K*-edge spectra.[104–106] Although the DOS are large for the empty $e_g^{\uparrow}$ and $t_{2g}^{\downarrow}$ bands, they are not directly accessible for *K*-edge absorption via dipole transitions. Thus, the main *K*-edge absorption begins where the large part of the $4p$ states is highly delocalized and extends over several Mn atoms. Takahashi *et al.*[107] show that the intensity of the Mn *K*-edge spectrum increases with an increasing degree of local lattice distortion and is insensitive to the magnetic order. The experimental Mn *K*-edge spectra show two peaks in the lower-energy region and these are well re-

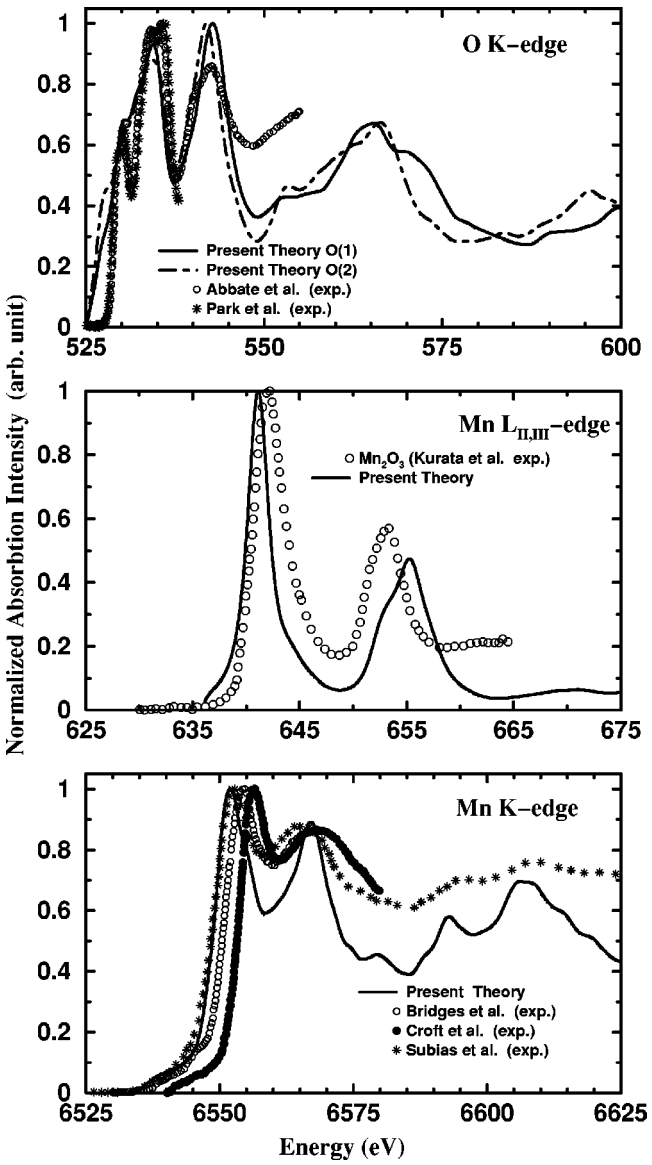

FIG. 12. XANES spectra for *A*-AF-state $LaMnO_3$ with orthorhombic $GdFeO_3$-type structure. The experimental Mn *K*-edge spectra are taken from Refs. 104–106, the Mn $L_{II,III}$ spectrum from Ref. 103, and the O *K*-edge spectra from Refs. 44 and 102.

produced in our theoretical spectrum. In particular our Mn *K*-edge spectrum is found to be in very good agreement with that of Subias *et al.*[104] in the whole energy range we have considered. The good agreement between experimental and calculated XANES spectra further emphasizes the relatively little significance of correlation effects in $LaMnO_3$ and also shows that the gradient-corrected full-potential approach is able to predict even the unoccupied states quite correctly.

IV. SUMMARY

Transition-metal oxides are generally regarded as a strongly correlated systems which are believed to be not properly treated by electronic structure theory. The present article has demonstrated, however, that accurate full-potential calculations including SO coupling and generalized-gradient corrections can account well for several features observed for $LaMnO_3$. We have presented a variety of results based on the *ab initio* local spin-density approach that are, broadly speaking, in agreement with experimental results for both ground- and excited-state properties. The present study strongly supports experimental[108–112] and theoretical models[13,17] in which a strong coupling of the conduction electrons to a local Jahn-Teller distortion is considered to be important for understanding the basic physical properties of manganites. In particular we found the following.

(1) The Mn ions are in the high-spin state in $LaMnO_3$ and hence the contributions to the minority-spin channel from the Mn $3d$ electrons are negligibly small.

(2) The Mn t_{2g} electrons are well localized and mainly participate in the magnetism. The e_g electrons are present in the entire valence-band region and they are mainly distributed near E_F in the VB. As the O states are not present in the vicinity of E_F the transport properties of hole-doped $LaMnO_3$ are dominated by Mn e_g electrons.

(3) The insulating behavior in $LaMnO_3$ originates from the combined effect of Jahn-Teller distortion and *A*-type antiferromagnetic ordering.

(4) Without Jahn-Teller distortion $LaMnO_3$ is predicted to be a ferromagnetic metal.

(5) Without inclusion of correlation effects in the calculations we are able to predict the correct *A*-type antiferromagnetic insulating ground state for $LaMnO_3$. This indicates that the importance of correlation effects has been exaggerated for this material.

(6) The large changes in energy and the development of an energy gap resulting from the structural distortion along with the exchange splitting indicate strong magnetostructural coupling. This may be the possible origin for the observation of CMR in hole-doped $LaMnO_3$.

(7) Our calculations support the viewpoint that the stabilization of the cubic phase is the prime cause for the occurrence of the ferromagnetic state by hole doping rather than the often believed double-exchange mechanism.

(8) The density-functional approach works well for not only the ground-state properties, but also the excited-state properties of $LaMnO_3$.

ACKNOWLEDGMENTS

P.R. is grateful for financial support from the Research Council of Norway. The authors wish to acknowledge Y. Tokura, T. Arima, K. Takenaka, and J. Jung for generously sending their experimental optical data for comparison. Part of these calculations was carried out on the Norwegian supercomputer facilities. We are grateful to Igor Solovyev and Lars Nordström for useful communications, to R. Vidya for comments and critical reading of the manuscript, and to John Wills, Karlheinz Schwarz, and Peter Blaha for making their programs available for the present study. O.E. is grateful to the Swedish Research Foundation and the Swedish Foundation for Strategic Research (SSF).

*Electronic address: ravindran.ponniah@kjemi.uio.no

[1] G. Jonker and J. Van Santen, Physica (Amsterdam) **16**, 337 (1950).
[2] E. O. Wollan and W. C. Koehler, Phys. Rev. **100**, 545 (1955); W. C. Koehler and E. O. Wollan, J. Phys. Chem. Solids **2**, 100 (1957).
[3] P. Schiffer, A. P. Ramirez, W. Bao, and S. W. Cheong, Phys. Rev. Lett. **75**, 3336 (1995).
[4] T. Mizokawa, D. I. Khomskii, and G. A. Sawatzky, Phys. Rev. B **60**, 7309 (1999).
[5] R. M. Kusters, J. Singleton, D. A. Keen, R. McGreevy, and W. Hages, Physica B **155**, 362 (1989); K. Chahara, T. Ohno, M. Kasai, and Y. Kozono, Appl. Phys. Lett. **63**, 1990 (1993); R. von Helmolt, J. Wecker, B. Holzapfel, L. Schultz, and K. Samwer, Phys. Rev. Lett. **71**, 2331 (1993); S. Jin, T. H. Tiefel, M. McCormack, R. A. Fastnacht, R. Ramesh, and L. Chen, Science **264**, 413 (1994); H. L. Ju, C. Kwon, R. L. Green, and T. Vankatesan, Appl. Phys. Lett. **65**, 2108 (1994).
[6] Y. Tomioka, A. Asamitsu, Y. Moritomo, H. Kuwahara, and Y. Tokura, Phys. Rev. Lett. **74**, 5108 (1995); P. Schiffer, A. P. Ramirez, W. Bao, and S.-W. Cheong, *ibid.* **75**, 3336 (1995); Y. Tomiaka, A. Asamitsu, Y. Moritomo, H. Kuwahara, and Y. Tokura, J. Phys. Soc. Jpn. **64**, 3626 (1995); H. Kuwahara, Y. Tomioka, A. Asamitsu, Y. Moritomo, and Y. Tokura, *ibid.* **64**, 3626 (1995).
[7] A. Asamitsu, Y. Moritomo, T. Arima, and Y. Tokura, Nature (London) **373**, 407 (1995); A. Asamitsu, Y. Moritomo, R. Kumai, Y. Tomioka, and Y. Tokura, Phys. Rev. B **54**, 1716 (1996).
[8] H. Y. Hwang, S.-W. Cheong, N. P. Ong, and B. Batlogg, Phys. Rev. Lett. **77**, 2041 (1996); T. Kimura, Y. Tomioka, H. Kuwahara, A. Asamitsu, M. Tamura, and Y. Tokura, Science **274**, 1698 (1996).
[9] C. Zener, Phys. Rev. **82**, 403 (1951); P. W. Anderson and H. Hasegawa, *ibid.* **100**, 675 (1955); P. G. de Gennes, *ibid.* **118**, 141 (1960).
[10] A. J. Millis, B. I. Shraiman, and R. Mueller, Phys. Rev. Lett. **77**, 175 (1996).
[11] M. Kataoka and M. Tachiki, Physica B **237-238**, 24 (1997).
[12] Y. Tokura, A. Urushibara, Y. Moritomo, T. Arima, A. Asamitsu, G. Kido, and N. Furukawa, J. Phys. Soc. Jpn. **63**, 3931 (1994).
[13] A. J Millis, P. B. Littlewood, and B. I. Shraiman, Phys. Rev. Lett. **74**, 5144 (1995); A. J. Millis, Phys. Rev. B **55**, 6405 (1997).
[14] K. I. Kugel and D. I. Khomski, Sov. Phys. JETP **37**, 725 (1973).
[15] R. Maezono, S. Ishihara, and N. Nagaosa, Phys. Rev. B **58**, 11 583 (1998).
[16] W. Koshibae, S. Ishihara, Y. Kawamura, S. Okamota, J. Inone, and S. Maekawa, Physica B **230-232**, 1058 (1997).
[17] H. Röder, J. Zang, and A. R. Bishop, Phys. Rev. Lett. **76**, 1356 (1996).
[18] S. Ishihara, M. Yamanaka, and N. Nagaosa, Phys. Rev. B **56**, 686 (1997).
[19] A. J. Millis, P. B. Littlewood, and B. I. Shraiman, Phys. Rev. Lett. **74**, 5144 (1995).
[20] P. E. de Brito and H. Shiba, Phys. Rev. B **57**, 1539 (1998).
[21] A. Takahashi and H. Shiba, Eur. Phys. J. B **5**, 413 (1998).
[22] Y. Motome and M. Imada, J. Phys. Soc. Jpn. **68**, 16 (1999).
[23] O. N. Mryasov, R. F. Sabiryanov, A. J. Freeman, and S. S. Jaswal, Phys. Rev. B **56**, 7255 (1997).
[24] Z. Popovic and S. Satpathy, Phys. Rev. Lett. **84**, 1603 (2000).
[25] I. V. Solovyev and K. Terakura, J. Korean Phys. Soc. **33**, 375 (1998).
[26] K. H. Ahn and A. J. Millis, J. Appl. Phys. **87**, 5013 (2000).
[27] I. Solovyev, N. Hamada, and K. Terakura, Phys. Rev. B **53**, 7158 (1996).
[28] J. F. Lawler, J. G. Lunney, and J. M. D. Coey, Appl. Phys. Lett. **65**, 3017 (1994).
[29] G. Pari, S. Mathi Jaya, G. Subramoniam, and R. Asokamani, Phys. Rev. B **51**, 16 575 (1995).
[30] Z. Yang, L. Ye, and X. Xie, J. Phys.: Condens. Matter **12**, 2737 (2000).
[31] V. I. Anisimov, J. Zaanen, and O. K. Andersen, Phys. Rev. B **44**, 943 (1991).
[32] I. V. Solovyev, P. H. Dederichs, and V. I. Anisimov, Phys. Rev. B **50**, 16 861 (1994).
[33] W. Y. Hu, M. C. Qian, Q. Q. Zheng, H. Q. Lin, and H. K. Wong, Phys. Rev. B **61**, 1223 (2000).
[34] S. Satpathy, Z. S. Popovic, and F. R. Vukajlovic, Phys. Rev. Lett. **76**, 960 (1996).
[35] K. Held and D. Vollhardt, Phys. Rev. Lett. **84**, 5168 (2000).
[36] J. Inoue and S. Maekawa, Phys. Rev. Lett. **74**, 3407 (1995).
[37] A. E. Bocquet, T. Mizokawa, T. Saitoh, H. Namatame, and A. Fujimori, Phys. Rev. B **46**, 3771 (1992).
[38] D. D. Sarma, N. Shanthi, and P. Mahadevan, Phys. Rev. B **54**, 1622 (1996).
[39] W. E. Pickett and D. J. Singh, Phys. Rev. B **53**, 1146 (1996).
[40] I. Solovyev, N. Hamada, and K. Terakura, Phys. Rev. Lett. **76**, 4825 (1996).
[41] D. D. Sarma, N. Shanthi, S. R. Barman, N. Hamada, H. Sawada, and K. Terakura, Phys. Rev. Lett. **75**, 1126 (1995).
[42] D. J. Singh and W. E. Pickett, Phys. Rev. B **57**, 88 (1998).
[43] M. Abbate, F. M. F. de Groot, J. C. Fuggle, A. Fujimori, O. Strebel, F. Lopez, M. Domke, G. Kaindl, G. A. Sawatzky, M. Takano, Y. Takeda, H. Eisaki, and S. Uchida, Phys. Rev. B **46**, 4511 (1992).
[44] J.-H. Park, C. T. Chen, S.-W. Cheong, W. Bao, G. Meigs, V. Chakarian, and Y. U. Idzerda, Phys. Rev. Lett. **76**, 4215 (1996).
[45] T. Saitoh, A. E. Bocquet, T. Mizokawa, H. Namatame, A. Fujimori, M. Abbate, Y. Takeda, and M. Takano, Phys. Rev. B **51**, 13 942 (1995).
[46] S. Bouarab, A. Vega, and M. A. Khan, Phys. Rev. B **54**, 11 271 (1996).
[47] H. Sawada, Y. Morikawa, K. Terakura, and N. Hamada, Phys. Rev. B **56**, 12 154 (1997).
[48] G. Matsumoto, J. Phys. Soc. Jpn. **29**, 606 (1970).
[49] J. B. A. A. Elemans, B. V. Laar, K. R. V. D. Veen, and B. O. Looptra, J. Solid State Chem. **3**, 238 (1971).
[50] J. B. Goodenough, Phys. Rev. **100**, 564 (1955).
[51] P. Blaha, K. Schwarz, and J. Luitz, WIEN97, Vienna University of Technology, 1997 [improved and updated Unix version of the original copyrighted WIEN code, which was published by P. Blaha, K. Schwarz, P. Sorantin, and S. B. Trickey, Comput. Phys. Commun. **59**, 399 (1990)].
[52] J. P. Perdew, K. Burke, and M. Ernzerhof, Phys. Rev. Lett. **77**, 3865 (1996).
[53] J. M. Wills, O. Eriksson, M. Alouani, and D. L. Price, in *Electronic Structure and Physical Properties of Solids*, edited by H. Dreysse (Springer, Berlin, 2000), p. 148; J. M. Wills and B. R.

Cooper, Phys. Rev. B **36**, 3809 (1987); D. L. Price and B. R. Cooper, *ibid.* **39**, 4945 (1989).
[54] O. K. Andersen, Phys. Rev. B **12**, 3060 (1975).
[55] M. Alouani and J. M. Wills, Phys. Rev. B **54**, 2480 (1996); R. Ahuja, S. Auluck, J. M. Wills, M. Alouani, B. Johansson, and O. Eriksson, Phys. Rev. B **55**, 4999 (1997).
[56] F. J. Kahn, P. S. Pershan, and J. P. Remeika, Phys. Rev. **186**, 891 (1969).
[57] M. Faraday, Philos. Trans. R. Soc. London **136**, 1 (1846).
[58] W. Reim and J. Schoenes, in *Ferromagnetic Materials*, edited by K. H. K. Buschow and E. P. Wohlfarth (Elsevier, Amsterdam, 1990), Vol. 5.
[59] H. Winter, P. J. Durham, and G. M. Stocks, J. Phys. F: Met. Phys. **14**, 1047 (1984).
[60] J. Redinger, P. Marksteiner, and P. Weinberger, Z. Phys. B: Condens. Matter **63**, 321 (1986).
[61] P. Marksteiner, P. Weinberger, R. C. Albers, A. M. Boring, and G. Schadler, Phys. Rev. B **34**, 6730 (1986).
[62] A. Neckel, K. Schwarz, R. Eibler, and P. Rastl, Microchim. Acta, Suppl. **6**, 257 (1975).
[63] T. Arima, Y. Tokura, and J. B. Torrance, Phys. Rev. B **48**, 17 006 (1993).
[64] J. Zaanen, G. A. Sawatzky, and J. W. Allen, Phys. Rev. Lett. **55**, 418 (1985).
[65] J. B. Goodenough, *Magnetism and the Chemical Bond* (Wiley, New York, 1963).
[66] Y. Okimoto, T. Katsufuji, T. Ishikawa, A. Urushibara, T. Arima, and Y. Tokura, Phys. Rev. Lett. **75**, 109 (1995).
[67] P. Mahadevan, N. Shanthi, and D. D. Sarma, J. Phys.: Condens. Matter **9**, 3129 (1997).
[68] N. Hamada, H. Sawada, and K. Terakura, in *Spectroscopy of Mott Insulators and Correlation Metals*, edited by A. Fujimori and Y. Tokura (Springer, Berlin, 1995).
[69] W. C. Koehler and E. O. Wollan, J. Phys. Chem. Solids **2**, 100 (1957).
[70] K. Terakura, I. V. Solovyev, and H. Sawada, in *Advances in Condensed Matter Science: Colossal Magnetoresistive Oxides*, edited by Y. Tokura (Gordon and Breach, Tokyo, 1999).
[71] K. Hirota, N. Kanedo, A. Nishizawa, and Y. Endoh, J. Phys. Soc. Jpn. **65**, 3736 (1996).
[72] F. Moussa, M. Hennion, J. Rodriguez-Carvajal, H. Moudden, L. Pinsard, and A. Revcolevschi, Phys. Rev. B **54**, 15 149 (1996).
[73] T. Hotta, S. Yunoki, M. Mayr, and E. Dagotto, Phys. Rev. B **60**, R15 009 (1999).
[74] B. C. Hauback, H. Fjellvåg, and N. Sakai, J. Solid State Chem. **124**, 43 (1996).
[75] R. L. Rasera and G. L. Catchen, Phys. Rev. B **58**, 3218 (1998).
[76] A. Urushibara, Y. Moritomo, T. Arima, A. Asamitsu, G. Kido, and Y. Tokura, Phys. Rev. B **51**, 14 103 (1995).
[77] H. Kawano, R. Kajimoto, M. Kubota, and H. Yoshizawa, Phys. Rev. B **53**, R14 709 (1996).
[78] Y. R. Shen, Phys. Rev. **133**, 511 (1964).
[79] J. O. Donnell, M. S. Rzchowski, J. N. Eckstein, and I. Bozovic, Appl. Phys. Lett. **72**, 1775 (1998).
[80] A. B. Shick, Phys. Rev. B **60**, 6254 (1999).
[81] Q. Huang, A. Santoro, J. W. Lynn, R. W. Erwin, J. A. Borchers, J. L. Peng, and R. L. Greene, Phys. Rev. B **55**, 14 987 (1997).
[82] T. J. A. Popma and M. G. J. Kamminga, Solid State Commun. **17**, 1073 (1975).
[83] R. A. de Groot, F. M. Mueller, P. G. van Engen, and K. H. J. Buschow, Phys. Rev. Lett. **50**, 2024 (1983).
[84] P. Ravindran, A. Delin, P. James, B. Johansson, J. M. Wills, R. Ahuja, and O. Eriksson, Phys. Rev. B **59**, 15 680 (1999).
[85] W. E. Pickett and D. J. Singh, J. Magn. Magn. Mater. **172**, 237 (1997).
[86] K. H. Kim, J. H. Jung, and T. W. Noh, Phys. Rev. Lett. **81**, 1517 (1998).
[87] J. J. Hamilton, E. L. Keatley, H. L. Ju, A. K. Raychaudhuri, V. N. Smolyaninova, and R. L. Greene, Phys. Rev. B **54**, 14 926 (1996).
[88] P. Ravindran *et al.* (unpublished).
[89] S. Yamaguchi, Y. Okimoto, K. Ishibashi, and Y. Tokura, Phys. Rev. B **58**, 6862 (1998).
[90] I. V. Solovyev, Phys. Rev. B **55**, 8060 (1997).
[91] J. H. Jung, K. H. Kim, K. J. Eom, T. W. Noh, E. J. Choi, J. Yu, Y. S. Kwon, and Y. Chung, Phys. Rev. B **55**, 15 489 (1997).
[92] K. Takenaka, K. Iida, Y. Sawaki, S. Sugai, Y. Moritomo, and A. Nakamura, J. Phys. Soc. Jpn. **68**, 1828 (1999).
[93] R. Mahendiran, S. K. Tiwary, A. K. Raychaudhuri, T. V. Ramakrishnan, R. Mahesh, N. Rangavittal, and C. N. R. Rao, Phys. Rev. B **53**, 3348 (1996).
[94] G. H. Jonker, Physica (Amsterdam) **20**, 1118 (1954).
[95] Z. Yang, Z. Huang, L. Ye, and X. Xie, Phys. Rev. B **60**, 15 674 (1999).
[96] T. Mizokawa and A. Fujimori, Phys. Rev. B **54**, 5368 (1996).
[97] J. H. Jung, K. H. Kim, T. W. Noh, E. J. Choi, and J. Yu, Phys. Rev. B **57**, R11 043 (1998).
[98] I. V. Solovyev (unpublished).
[99] K. Takenaka, K. Iida, Y. Sawaki, S. Sugai, Y. Moritomo, and A. Nakamura, Phys. Status Solidi B **215**, 637 (1999).
[100] A. Chainani, M. Mathew, and D. D. Sarma, Phys. Rev. B **47**, 15 397 (1993).
[101] W. Speier, R. Zeller, and J. C. Fuggle, Phys. Rev. B **32**, 3597 (1985).
[102] M. Abbate, G. Zampieri, F. Prado, A. Caneiro, and A. R. B. Castro, Solid State Commun. **111**, 437 (1999).
[103] H. Kurata, E. Lefevre, C. Colliex, and R. Brydson, Phys. Rev. B **47**, 13 763 (1993).
[104] G. Subias, J. Garcia, J. Blasco, and M. G. Proietti, Phys. Rev. B **58**, 9287 (1998).
[105] F. Bridges, C. H. Booth, G. H. Kwei, J. J. Neumeier, and G. A. Sawatzky, Phys. Rev. B **61**, R9237 (2000).
[106] M. Croft, D. Sills, M. Greenblatt, C. Lee, S.-W. Cheong, K. V. Ramanujachary, and D. Tran, Phys. Rev. B **55**, 8726 (1997).
[107] M. Takahashi, J. Igarashi, and P. Fulde, J. Phys. Soc. Jpn. **68**, 2530 (1999).
[108] G. M. Zhao, K. Ghosh, H. Keller, and R. L. Greene, Phys. Rev. B **59**, 81 (1999).
[109] S. J. L. Billinge, R. G. Difrancesco, G. H. Kwei, J. J. Neumeier, and J. D. Thompson, Phys. Rev. Lett. **77**, 715 (1996).
[110] M. Jaime, M. B. Salamon, M. Rubenstein, R. E. Treece, J. S. Horwitz, and D. B. Chrisey, Phys. Rev. B **54**, 11 914 (1996).
[111] T. T. M. Palstra, A. P. Ramirez, S. W. Cheong, B. R. Zegarski, P. Schiffer, and J. Zaanen, Phys. Rev. B **56**, 5104 (1997).
[112] C. H. Booth, F. Bridges, G. H. Kwei, J. M. Lawrence, A. L. Cornelius, and J. J. Neumeier, Phys. Rev. Lett. **80**, 853 (1998).